Journal of the Meteorological Society of Japan

EARLY ONLINE RELEASE

The DOI for this manuscript is

DOI:10.2151/jmsj.2025-003

J-STAGE Advance published date: October 21, 2024

The final manuscript after publication will replace the preliminary version at the above DOI once it is available.

Synoptic- and meso-scale features of the heavy wet snow accretion event along the Okhotsk Sea coast on December 22–23, 2022

Yuki Kanno[1], Soichiro Sugimoto[1], and Masataka Murakami[2, 3]

1: *Sustainable System Research Laboratory, Central Research Institute of Electric Power Industry, Abiko, Japan*

2: *Institute for Space-Earth Environmental Research, Nagoya University, Nagoya, Japan*

3: *Meteorological Research Institute, Japan Meteorological Agency, Tsukuba, Japan*

Submitted to JMSJ

Corresponding author: Yuki Kanno, Sustainable System Research Laboratory, Central Research Institute of Electric Power Industry, 1646 Abiko, Abiko-shi, Chiba, 270-1194, Japan.

E-mail: kanno3830@criepi.denken.or.jp

Abstract

Heavy wet snow accretion occurred along the coast of the Okhotsk Sea, collapsing a transmission tower near Monbetsu City and causing a power outage in the area, on December 22–23, 2022. This study investigated the meteorological conditions that caused heavy wet snow accretion in this area, with a particular focus on three factors responsible for wet snow accretion: strong winds, snowfall, and temperatures slightly above 0 °C. An analysis of the station observations from the Japan Meteorological Agency shows that this case occurred on the most favorable day for the wet snow accretion in Hokkaido since 1976. A duration of favorable temperatures for wet snow accretion for this case was longer than historical events by 30%. A numerical simulation using the Weather Research and Forecasting model, with a horizontal resolution of 1.667 km, demonstrated that the formation of torrential wet snowfall and strong winds were associated with multiple extratropical cyclones. On the evening of December 22, a cyclone moving northward off the eastern coast of Japan, together with another stagnant cyclone located over the northern Japan Sea, formed a large cyclonic circulation. The cold conveyor belt, a cold airstream located poleward of the warm front, associated with the northward-moving cyclone, caused strong easterly winds along the coast of the Okhotsk Sea and carried a large amount of moisture there, reinforcing snowfall from stratiform clouds through depositional growth. A backward trajectory analysis showed that temperatures slightly above 0 °C were maintained through the balance between heating from the sea surface and cooling caused by snow melting. The norward-moving cyclone tracks resembled other historical events at Monbetsu, but the precipitation amounts were the largest in this event. These findings suggest that a combination of synoptic-scale circulations and cloud microphysics plays an essential role in the occurrence of heavy wet snow accretion.

Keywords: snow accretion, extratropical cyclone, numerical simulation, snow melting, trajectory analysis

1. Introduction

Atmospheric icing refers to the accretion of solid precipitation particles onto the surfaces of structures (Farzaneh 2008). In snowfall regions, severe icing causes disasters, such as the collapse of structures or trees, traffic disruptions, and power outages. Atmospheric icing can be classified as precipitation icing or in-cloud icing. The former includes wet and dry snow accretion and freezing rain. Wet snow accretion is a phenomenon in which partially melted snow sticks to structures due to strong winds at temperatures slightly above 0 °C (Takeuchi 1978; Farzaneh 2008).

Previous studies have examined the weather conditions that cause wet snow accretion on overhead power line conductors (Makkonen 1989; Sakamoto 2000; Bonelli et al. 2011; Nygaard et al. 2013; Ducloux and Nygaard 2014). Various criteria are used for the temperature range suitable for wet snow accretion, such as temperatures of 0–2 °C (Admirat 2008), the web bulb temperature of 0–1 °C (Nygaard et al. 2013), and a mixture of temperature and humidity criteria (Ducloux and Nygaard 2014). Although wet snow accretion onto the surface of structures may occur at any wind speed, the amount accreted increases with wind speed (Wakahama et al. 1977). The amount of snow accreted can be estimated from the amount of collisional precipitation on the surface of structures at temperatures slightly above 0 °C, referred to as the snow accretion potential. Disasters associated with wet snow accretion have been reported in extratropical countries including Japan, France, Germany, and North America (Wakahama et al. 1977; CIGRE 2006; Dalle and Admirat 2011; Frick and Wernli 2012; Hanesiak et al. 2022). In Japan, wet snow accretion occurs everywhere, except on the Ryukyu Islands.

In particular, precipitation in the temperature range suitable for snow accretion tends to be accompanied by strong winds in the Pacific coastal region of the Kanto area and eastern Hokkaido (Matsushita and Nishio 2006).

Most cases of snow damage associated with wet snow accretion in Japan have been caused by extratropical cyclones approaching Japan during the cold season, such as in Northern Hokkaido in December 1972, in the Tohoku area in December 1980, in the Kanto area in March 1986, and in the Hokuriku area in December 2005 (Hasemi and Baba 1994; Ohara et al. 2017). As extratropical cyclones have a strong pressure gradient, their approach causes strong winds. Precipitation accompanied by extratropical cyclones is closely related to their air flow structure. Extratropical cyclones have the following three distinct air flows: warm conveyor belt (WCB), cold conveyor belt (CCB), and dry intrusion (Carlson 1980; Browning 1986). The WCB is a poleward, coherent, warm, and moist airstream originating in the planetary boundary layers of the warm sector of an extratropical cyclone. Air masses in the WCB ascend to the upper troposphere within two days (Madonna et al. 2014). The CCB is a low-level westward airstream of cold air masses poleward of the warm front towards the center of the extratropical cyclone. Precipitation accompanied by extratropical cyclones is closely related to both the WCB and CCB. Ascending air masses in the WCB along isentropes sloping northward in the warm front lead to the formation of stratiform clouds, which are then advected by mid- and upper-level winds, eventually forming deep stratiform clouds that expand north of the warm front (Browning 1986; Neiman et al. 1993). The heavy precipitation zone expanding north of the warm front is known as the warm frontal rainband (Houze et al. 1976). Highly concentrated ice crystals in the generating cells located above the stratiform clouds of the warm frontal rainband grow through aggregation, riming, and deposition of water vapor and eventually fall (Hobbs and Locatelli 1978). As falling ice crystals in the warm frontal rainband must pass through the CCB, the temperature and humidity of the CCB are important for controlling the type and amount of surface precipitation (Schultz 2001).

On December 22, 2022, an extratropical cyclone that moved northward off the east coast of the main island of Japan caused heavy snowfall and strong winds along the coast of the Okhotsk Sea in Hokkaido and led to traffic disruptions. Additionally, heavy wet snow accretion on overhead power lines initiated the collapse of a transmission tower in Monbetsu, a coastal city facing the Okhotsk Sea (Fig. 1), causing a 20 h blackout in the area, including approximately 28,000 houses (Cabinet Office 2023). This study aimed to investigate the meteorological conditions that caused heavy snow accretion along the Okhotsk Sea coast from analyses of a reanalysis dataset, observational data, and simulation data using a non-hydrostatic meso-scale model. The study specifically focused on the three major factors causing wet snow accretion: strong winds, snowfall, and a temperature range favorable for wet snow accretion.

The remainder of this paper is organized as follows. Section 2 describes the methodology and data used in this study. Section 3 overviews the meteorological situations. Section 4 discusses the characteristics of cloud systems that caused heavy snow accretion. Section 5 presents the formation mechanism of the temperature range suitable for wet snow accretion. Section 6 compares this case with similar historical events. Finally, Section 7 presents concluding remarks.

2. Data and Methods

2.1. Data

The ERA5 reanalysis dataset (Hersbach et al. 2020) was used to examine synoptic-scale circulation at upper levels and as the initial and boundary conditions for numerical simulations. Mean sea level pressure, temperature, geopotential height, and zonal and meridional winds at 37 pressure levels with a horizontal resolution of 0.25° were used. Divergence was derived from the zonal and meridional winds. Hourly surface observations from the Automated Meteorological Data Acquisition System (AMeDAS), managed by the Japan Meteorological Agency, were obtained from 1976 to 2022. Temperature, 10-minute averaged wind speed and direction, sunshine duration, precipitation amount, snowfall amount, and snow depth were obtained from AMeDAS. Rain gauges used in AMeDAS are equipped with heaters to measure precipitation from solid precipitation. In some AMeDAS stations, the anemometer is installed at a height higher than 10 m above the ground in order to avoid the influence of surrounding artificial structures. A logarithmic law was used to estimate wind speed at a 10-m height based on data from the AMeDAS. We used 100-m-meshed land-use data from the National Land Numerical Information (NLNI) database, updated in 1976, 1987, 1991, 1997, 2006, 2009, 2014, and 2016, as an indicator of the ground roughness length. Following Kondo and

Yamazawa (1986), the roughness length was estimated using the NLNI land-use database by averaging the roughness classification over a windward fan-shaped area with a central angle of 45° and the radius that is calculated by multiplying 100 to the height of an anemometer.

2.2. Configuration of numerical simulation

The Weather Research and Forecasting (WRF) model, version 4.4.2 (Skamarock et al. 2021), was used to examine the precipitation and local temperature characteristics. The simulation was conducted using two domains with one-way nesting. The outer domain (D1) covered the Northwestern Pacific with a horizontal resolution of 5 km, and the inner domain (D2) had a horizontal resolution of 1.667 km (Fig. 2). We present the results from the inner domain as a control simulation. The model had 45 vertical layers with a top pressure of 50 hPa. The atmospheric initial and boundary conditions for the outer domain, as well as sea surface temperature (SST) and sea-ice concentrations, were obtained from the ERA5 reanalysis dataset. The WRF default topography dataset, GTOPO30, was used. The simulation of the outer domain spanned 06 JST on December 22 to 18 JST on December 23, 2022. Simulation of the inner domain began 3 h after the start of the outer domain. The physics parameterizations included the Eta similarity (Janjić 1990), RUC land-surface model (Benjamin et al. 2004), and Mellor-Yamada-Janjic (Janjić 1994) schemes for the surface, land surface, and planetary boundary layer (PBL), respectively, along with the predicted particle properties (P3) scheme with two free ice categories (Morrison and Milbrandt 2015; Milbrandt and Morrison 2016), the multi-scale

Kain-Fritsch scheme applied only to the outer domain (Zheng et al. 2016), and the rapid radiative transfer model for GCMs (RRTMG; Iacono et al. 2008). Table 1 lists the model configurations. To explain the maintenance mechanism of temperatures suitable for wet snow accretion at Monbetsu, heating rates from the parameterizations (radiation, PBL, and cloud microphysics) and cloud microphysics processes in the control simulation were analyzed. The latter was obtained by modifying the P3 microphysics scheme to output mixing ratio budget terms.

Furthermore, we conducted an additional simulation to examine the role of melting processes for the maintenance of temperatures suitable for wet snow accretion. As a sensitivity experiment, we excluded the cooling of the melting solid hydrometers from the temperature budget equation in the P3 microphysics scheme. This sensitivity experiment is referred to as the no-melt-heating simulation. Other settings were identical to the control simulation.

2.3. Trajectory analysis

To elucidate the maintenance mechanism of an favorable temperature range for wet snow accretion, a backward trajectory analysis of air parcels that arrived in Monbetsu was conducted. LAGRANTO (Sprenger and Wernli 2015) was used to compute backward trajectories from the control simulation. LAGRANTO computes three-dimensional kinematic trajectories from three-dimensional wind fields and the meteorological parameters at the parcel locations in the control simulation. A total of 54 air parcels were placed in nine grids centered on the grid points nearest Monbetsu Station, at heights of 50, 100, 150, 200, 250, and 300 m.

2.4. Estimation of the scale of wet snow accretion

A simple version of the snow accretion potential (SAP) defined by Shimizu et al. (2017) was introduced to understand the sensitivity of wet snow accretion. The SAP [kg m^{-2}] is defined as follows:

$$\mathrm{SAP} = \rho_w \beta P_i, \tag{1}$$

where ρ_w(=1,000 kg m^{-3}) is the density of liquid water, β is the snow accretion efficiency, and P_i [mm h^{-1}] is the amount of precipitation that collides with an electrical wire in unit time. Here, β is originally a product of a term of snowflake wetness and correction associated with wind speed. The snowflake wetness term is estimated based on the relationship among wetness, temperature, and relative humidity (Matsuo et al. 1981). As relative humidity observations are available only in a few AMeDAS stations, the simplified SAP assumes that β depends only on temperature, as follows:

$$\beta = \begin{cases} 1 & (0^\circ\mathrm{C} \le T \le 2^\circ\mathrm{C}) \\ 0 & (T < 0^\circ\mathrm{C} \text{ or } T > 2^\circ\mathrm{C}). \end{cases} \tag{2}$$

In Eq. (1), P_i can be written as follows:

$$P_i = \frac{P V_n}{v_T}, \tag{3}$$

where P [mm h^{-1}] is the hourly precipitation rate and V_n [m s^{-1}] is the collisional speed of precipitation particles perpendicular to a certain wire in the power lines, calculated as follows:

$$V_n = \sqrt{v_T^2 + (U \sin\theta)^2}, \tag{4}$$

where θ is the angle between the electrical wire and horizontal wind direction. As this analysis does not intend to estimate the value for any specific transmission line, $\theta = 90^{\circ}$ was used in the calculation. Further, v_T [m s^{-1}] is the falling speed of a precipitation particle, assumed a constant value of 1.5 m s^{-1} based on observational studies (Locatelli and Hobbs 1974; Mitra et al. 1990; Frick et al. 2013). Parameter U [m s^{-1}] is the horizontal wind speed at a 10-m height, estimated from AMeDAS. The hourly precipitation in Eq. (3) was corrected for wet snow as follows:

$$P = P_{obs}(1 + 0.115V), \quad (5)$$

where V [m s^{-1}] is the wind speed corrected to a value at the height of the rain gauge, estimated in the same manner mentioned above. Following Shimizu et al. (2017), the shedding of accreted wet snow on an electric wire occurs when either of the following two conditions is met: (1) the 3-h sum of the hourly temperature exceeds $4\,^{\circ}\mathrm{C}$ or (2) no precipitation is observed for more than 6 h.

2.5. Cyclone detection and tracking

To compare cyclone tracks for wet snow accretion at Monbetsu during historical events, we used the University of Melbourne cyclone detection and tracking algorithm (Murray and Simmonds 1991a, 1991b). This algorithm detects cyclones as the local maxima in the Laplacian of mean sea level pressure and tracks them over time. In the tracking, a nearest-neighbor method is employed. The 3-h mean-sea level pressure from the ERA5 was used for the detection. We detected cyclones in the Northern Hemisphere, but we focused only on the one closest to Monbetsu during high SAP value events. Parameters used for the detection and tracking algorithms are summarized in Appendix.

3. Case overview

3.1. Synoptic circulations

Several extratropical cyclones were located around Japan on December 22 and 23, 2022. An extratropical cyclone at 110° E and 45° N at 15 JST on December 19 moved eastward and remained over the Japan Sea from 15 JST on December 21 to 03 JST on December 24 (hereafter, this cyclone is called C1). The C1 cyclone developed with a decrease in its surface pressure from 994 hPa at 09 JST on December 22 to 980 hPa at 09 JST on December 23 (Figs. 3a and 3c). To the west of the C1 cyclone, a cut-off low at 500 hPa was located around the base of the Korean Peninsula (Fig. 4a). The interaction between the surface and upper cyclones contributed to the baroclinic development of C1. The temperature at 850 hPa at 09 JST on December 22 shows that the temperatures between -6 and 0 °C zone extended eastward and southward from the C1 cyclone with a large gradient (Fig. 4b), suggesting the existence of warm and cold fronts.

At 09 JST on December 22, two extratropical cyclones consisting of a north–south pair were detected south of Honshu Island (Fig. 3a). The northern cyclone was located on the southern coast of the main island of Japan (hereafter, called C2) and in the warm sector of cyclone C1. The C2 cyclone moved northward and reached the south of Cape Erimo at 21 JST on December 22 (Fig. 3b). It slowly landed at eastern Hokkaido with a decrease in the central pressure of 20 hPa for 24 h until 09 JST on December 23 (Fig. 3c). Simultaneously, a zonally elongated area of upper-level divergence over the

Japan Sea and Hokkaido indicates that diabatic heating near the center of the C1 and C2 cyclones contributed to their rapid development. The track of the C2 cyclone is illustrated in Fig. 3d using the cyclone tracking algorithm and corresponds to the south-coast cyclone that travelled towards eastern Hokkaido (Yoshida and Asuma 2004; Tsopouridis et al. 2020). Furthermore, an extratropical cyclone located over eastern Hokkaido is known to caused heavy snowfall in the coastal areas of the Okhotsk Sea (Kawazoe et al. 2020). A sharp gradient of temperatures between 6 and 12 °C corresponded to the warm and cold fronts of the C2 cyclone. On the night of December 22, a new extratropical cyclone was found at the occluded point of the C2 cyclone (hereafter, called C3). The C3 cyclone was located southeast of the C2 cyclone at 09 JST on December 23.

The extratropical cyclone, located at 30 °N and 142 °E at 09 JST on December 22, moved northeastward and away from Hokkaido. Corresponding to the three cyclones aligned southeast of eastern Hokkaido, the upper-level divergence was elongated from northwest to southeast (Fig. 4e). From the evening of December 22 to 24, cyclones C1 to C4 formed a large cyclonic circulation centered over northern Japan. The interval between the isobars was narrow near the center of cyclonic circulation. Strong easterly surface winds exceeding 15 m s^{-1} were analyzed over the Okhotsk Sea from 21 JST on December 22 to 21 JST on December 23 in the ERA5 reanalysis (Figs. 3b-3d).

3.2. Local meteorological characteristics from surface observations

To examine the spatial distributions of the surface meteorological fields associated with wet snow accretion, Figures 5a-5c show the 24-h accumulated precipitation, maximum wind speed, and temperature observed at AMeDAS stations, respectively. In Fig. 5b, the maximum wind speed was corrected for a 10-m height. The spatial patterns of the 24-h accumulated precipitation until 15 JST on December 23 (Fig. 5a) show that precipitation was concentrated in eastern Hokkaido, consistent with the fact that precipitation was accompanied by a northward moving extratropical cyclone. However, the accumulated precipitation near the coast of the Okhotsk Sea was less than 40 mm. Strong winds exceeding 10 m s^{-1} were observed along the coasts of the Okhotsk Sea and the Pacific Ocean (Fig. 5b). The average surface temperature over 24 h had a suitable range for wet snow accretion, between 0 and 2 °C, at most Hokkaido stations, except for highly elevated stations (Fig. 5c).

The spatial pattern of the 24-h accumulated SAP differed from the precipitation pattern (Fig. 5d). High SAP values were analyzed along the coast of the Okhotsk Sea and eastern Hokkaido. The SAP in Monbetsu station calculated using Eq. (1) was 429.7 kg m^{-2}, the 4th highest in Hokkaido for this event. This result suggests that the surface weather conditions along the Okhotsk Sea were favorable for the occurrence of wet snow accretion.

To demonstrate the suitability of the meteorological conditions in this case for wet snow accretion, the SAP was calculated from AMeDAS data since 1976 and compared with that in this case. Shedding conditions were applied for this calculation. Since 1976, the SAP values in the current case were 12th, 13th, 14th, and 35th at Omu, Kushiro, Nakashibetsu, and Monbetsu stations, respectively. The number of stations among the top 50 wet snow accretion indices since 1976 was the highest for this case, with seven stations, followed by four stations on December 7, 2007. Another interesting characteristic of this case was the prolonged persistence of a non-zero SAP. The average persistence of the wet snow accretion potential was 18.57 h in the current case, 30% longer than the average persistence of 14.16 h in the top 50 events. These results suggest that the meteorological conditions in this case were highly suitable for wet snow accretion over the last 50 years and persisted for longer periods.

Figure 6 shows the time-series of the surface observations at Monbetsu station from AMeDAS. Precipitation was observed between 19 JST on December 22 and 15 JST on December 23 (Fig. 6c). During this period, snow or the mixture of rain and snow were observed without sunshine (Figs 6b, 6d, and 6g). The hourly precipitation rate was between 1 and 5 mm h^{-1}, the accumulated precipitation was 56.5 mm until 15 JST on December 23, and the snow depth increased by 17 cm (Fig. 6e). Although precipitation measurements were not available after 15 JST on December 23, possibly due to blackout, snowfall was not suspected to be heavy because the snow depth decreased after 15 JST on December 23. During the snowfall period, the temperatures were slightly above 0 °C (Fig. 6a). The temperatures before and after the snowfall period were higher than those during the snowfall. Easterly winds of 5–8 m s^{-1} were observed from 12 JST on December 22 to 02 JST on December 23 (Figs. 6f and 6g). Subsequently, the wind direction changed anticlockwise, and northerly winds of 6–10 m s^{-1} occurred on the afternoon of December 23. These findings confirm that the meteorological conditions in Monbetsu city were suitable for the occurrence of wet snow accretion.

4. Characteristics of precipitation systems

The characteristics of the precipitation system that caused heavy wet snow accretion along the coast of the Okhotsk Sea were examined by the numerical simulations using a WRF model with a horizontal resolution of 1.667 km. Before examining precipitation characteristics, the reproducibility of the numerical simulation was verified. Figure 7 shows a comparison of the (a) wind direction, (b) wind speed, (c) accumulated precipitation, (d) temperature, and (e) hourly SAP at Monbetsu Station between the AMeDAS observations and control simulation. Table 2 summarizes their bias and root mean square errors (RMSEs). Height correction was performed for the temperature using the temperature lapse rate between the lowest two model layers.

Overall, the control simulation accurately reproduced the meteorological conditions in terms of the occurrence of wet snow accretion. The gradual counterclockwise change in the wind direction from easterly to northerly was well simulated (Fig. 7a); however the simulated wind speed was overestimated with a positive bias of 2.0 m s^{-1} (Fig. 7b and Table 2). Previous studies have reported the tendency of wind speed overestimation with the Mellor-Yamada-Janjic PBL scheme (e.g., Shimada et al. 2011; Gómez-Navarro et al. 2015). In both the observations and simulations, precipitation began approximately 21 JST on December 22. Although the accumulated precipitation until 03 JST on December 23 calculated by numerical simulation was low, the accumulated precipitation at 15 JST on December 23 differed by less than 2.5 mm (Fig. 7c). The bias and RMSE of the precipitation rate were -0.11 and 1.30 mm h^{-1}, respectively. During the precipitation period, the simulated surface temperature matched well with the observed temperature (Fig. 7d), with a bias of -0.01 °C and RMSE of 0.37 °C. The hourly SAP fluctuated between 10 and 50 kg m^{-2} h^{-1} (Fig. 7e). Overprediction (underprediction) occurred in the control simulation for 0-3 (6-9) JST on December 23 because the hourly precipitation rate was overpredicted (underpredicted) for this period, resulting in a small bias of -2.15 kg m^{-1} h^{-1}. These results confirms that the control simulation well reproduced the meteorological variables associated with wet snow accretion.

Figure 8 shows the simulated equivalent radar reflectivity (hereafter, reflectivity) at an altitude of 2 km. At 21 JST on December 22, a high-reflectivity region with small spatial variations expanded to eastern Hokkaido, north of the C2 cyclone, indicating stratiform clouds (Fig. 8a). The tops of the stratiform clouds reached 8 km (Fig. 9). At 03 JST on December 23, the head of the comma-shaped clouds near the center of C2 cyclone approached the coastal area facing the Okhotsk Sea (Fig. 8b). Monbetsu city was covered by convective clouds, with cloud tops as low as 4 km (Fig. 9). At 10 and 13 JST on December 23, clouds expanded zonally from both the C1 and C2 cyclones, but the reflectivity value was smaller than that at 21 JST on December 22 (Figs. 8c and 8d). This indicates that the observed snow or the mixture of rain and snow fell from stratiform clouds in the earlier period, convective clouds in the middle period, and stratiform clouds in the later period. Furthermore, the 0 °C line was simulated 100 m above sea level during the precipitation periods (Fig. 9), consistent with the observed rain/snow mixture.

To examine the relationship between the characteristics of clouds accompanied by the C1 cyclone and environmental fields, Fig. 10a shows the vertically integrated vapor transport at 00 JST on December 23, when the precipitation is intensified. Figure 10b shows that a substantial amount of water vapor with a mixing ratio exceeding 5 g kg^{-1} was transported northward in the warm sector of the C1 cyclone, corresponding to the WCB of the C2 cyclone. Water vapor in the WCB ascended along the isentropes, tilting northward in warm and occluded fronts (Fig. 10b), and subsequently condensated, leading to the formation of stratiform clouds (Fig. 8a). The stratiform clouds were advected northward due to mid-level southerly winds (Fig. 10c). Even in the north of the C2 cyclone, water vapor with a mixing ratio exceeding 3 g kg^{-1} was transported westward towards the north of the C1 cyclone, indicating that the CCB of C2 cyclone also contributed to vapor transport.

The westward moisture transport by the CCB of the C2 cyclone affected the microphysics of the snowfall in the stratiform clouds. A meridional-vertical cross-section of the simulated reflectivity across Monbetsu city shows high reflectivity below an altitude of 4 km, where the vapor mixing ratio is high (Figs. 10c and 10d). This is attributed to the high mixing ratio of the solid hydrometers (Fig. 10e). In the P3 scheme, four parameters (mass, rime mass, rime volume, and number) were predicted for each free ice category instead of categorizing solid hydrometers into ice crystals, snow, and graupel (Morrison and Milbrandt 2015). The riming fraction, which is the fraction of the mixing ratio obtained by riming to the total, was close to zero, suggesting that the solid hydrometers grew as a result of depositional growth of water vapor (Fig. 10f). The source and sink terms of the sum of the two ice categories in Fig. 11a confirm that the ice mixing ratio increased due to depositional growth below an altitude of 4 km, where air masses were nearly saturated with respect to liquid water (Fig. 12a). These results suggest that the nearly saturated CCB reinforced snowfall through the depositional growth of ice crystals and snowflakes.

As the C2 cyclone moved northward, the coastal area of the Okhotsk Sea was covered with convective clouds near the center of the cyclone at 03 JST on December 23. Similar to 21 JST on December 22, water vapor was transported westward to the north of the C1 cyclone at 03 JST on December 23 (Fig. 13a). In the Monbetsu area, the wind direction changed clockwise from easterly to southeasterly with increasing height, up to an altitude of 5 km (Fig. 13c). The mixing ratio of rain was higher in convective clouds at 03 JST on December 23 than in stratiform clouds at 21 JST on December 22 (Figs. 10e and 13e). The cloud droplets were transported upward above the melting level by updrafts near the cyclone center (Fig. 13b), and the rain mixing ratio increased through the collection of cloud droplets (figure not shown). The high riming fraction was consistent with the characteristics of convective clouds (Fig. 13f). At lower levels, solid hydrometers grew through collisions with raindrops (Fig. 11b). The low cloud tops during this period could be explained by the vertical profile of the equivalent potential temperature. Air was saturated below an altitude of 3.5 km, whereas the vapor mixing ratio was almost zero above 5 km (Fig. 12b). This suggests that the intrusion of the stratospheric dry air mass behind the cold front acted as a lid for convective clouds.

At 13 JST on December 23, the coastal area of the Okhotsk Sea was covered with stratiform clouds. The center of the C2 cyclone was located near the coastal area of the Okhotsk Sea, and northeasterly winds prevailed in the Monbetsu area (Figs. 14a and 14b). The vapor mixing ratio decreased to 2 g kg^{-1} at this time (Fig. 14b). The longitude-altitude cross-section of reflectivity and ice mixing ratio across Monbetsu shows that clouds were covered below 4 km over northern Hokkaido (Figs. 14d and 14e). The mixing ratio of the solid hydrometers was high below 2 km and increased through the accretion of cloud droplets (Fig. 11c). This is consistent with the high riming fraction below an altitude of 2 km (Fig. 14f).

To explain the above analyses, the following hypotheses are suggested. First, snowfall resulted from the northward-moving C2 cyclone. Second, snowfall from the stratiform clouds was reinforced by westward vapor transport by the CCB of the C2 cyclone in the earlier period. Third, the snowfall type transition possibly occurred twice: initially unrimed snowflakes to rimed snowflakes fell from convective clouds approximately 03 JST on December 23, and subsequently changing to rimed snowflakes that collided with cloud droplets during the fell from stratiform clouds after the morning of December 23.

5. Maintenance mechanism of temperatures suitable for wet snow accretion

During snowfall, surface temperatures in the Monbetsu area persisted slightly above 0 °C, which are favorable for wet snow accretion. To reveal the mechanism for maintaining the temperatures favorable for wet snow accretion, a backward trajectory analysis of air parcels arriving at Monbetsu Station was performed using LAGRANTO. Figure 15a shows the pathways of the trajectories arriving at Monbetsu Station at 14 JST on December 23, 2022. The air parcels were located 500 m above the Kuril Islands, moved southward at 21 h, and turned west at 15 h before arrival. After passing through Etorofu Island, they entered the Okhotsk Sea 6 h before arrival. Over the Okhotsk Sea, the parcels were located at altitudes of less than 100 m. The spread in the trajectory paths was small.

Figures 15b–15e and 16 show the changes in the meteorological variables and heating rates along the trajectories, respectively. The SST was higher than the air parcel temperature by 4–5 °C prior to 3 h of arrival, except for the period between 5 h and 4 h, when the air parcels were across the Etorofu Islands (Fig. 15d). Heating from the PBL scheme represents the vertical diffusion of heat within the PBL to mitigate unstable conditions when the lowermost layer of the atmosphere (height of approximately 23 m) is heated from the sea surface (Fig. 16a). This heating increases the potential temperature of the air parcels by 3 °C for 12 h. Five hours before arrival, air parcels were located below an altitude of 100 m, and strong heating of air parcels at a rate of 3 °C per hour was largely cancelled by cooling from cloud microphysical processes, resulting in a net heating of 2 K per 6 h (Fig. 15c). A breakdown of the heating/cooling by cloud microphysical processes shows that melting of the solid hydrometers accounts for the aforementioned cooling (Fig. 16b). We also verified the sensitivity of the parcel locations and heating rates to the release time of the trajectory calculation. The route and abovementioned cancellation of heating rates were consistent for air parcels released after 22 JST on December 22. These results suggest that the cancellation of heating from the sea surface by cooling from the melting of solid hydrometers is crucial for maintaining a suitable temperature for wet snow accretion.

To further examine the role of the melting of solid hydrometers, a sensitivity experiment was conducted, where temperature changes associated with the melting of the solid hydrometers were excluded in the microphysics scheme. Figure 17 shows the time-series of observed and simulated surface temperatures at Monbetsu Station. Note that the time-series of the control simulation depicted in Fig. 17 is the same as that in Fig. 7d. The temperature in the no-melt-heating simulation was higher than that in the control simulation by 0.5–1 °C and was above 1 °C after 02 JST on December 23. This 1 °C difference could be essential for the occurrence of wet snow accretion. Previous field observations of wet snow accretion on electrical wires performed at Kushiro from 2010 to 2015 showed that wet snow accretions were observed at temperatures of 0–1 °C for a relative humidity exceeding 95%, whereas they were not observed for temperatures above 1 °C (Nishihara et al. 2017). These results indicate that cooling due to the melting of solid hydrometers plays an important role in the maintenance of a temperature suitable for wet snow accretion.

6. Historical context

To place this event in a historical context, we conducted a comparative analysis of the 10 highest SAP events at Monbetsu. Table 3 summarizes the 10 highest SAP events at Monbetsu. Four out of 10 cases occurred in winter, 5 in spring, and 1 in autumn. Among these 10 events, the December 2022 case was ranked first and characterized by the highest precipitation amount and third longest duration.

The maximum wind speed was not stronger than that in the other cases and was thus ranked fifth. This suggests that the highest precipitation amount during temperatures suitable for wet snow accretion contributed to the highest SAP value for this case.

For these 10 cases, extratropical cyclones were located over or off of the southeast point of eastern Hokkaido. Figure 18a illustrates the tracks of the extratropical cyclones that were in closest proximity to Monbetsu at the time of each event, using the University of Melbourne cyclone detection and tracking algorithm. The cyclone track for this case was similar to those for April 28 and 11, 2000, May 10, 1996, January 7, 2007, and November 27, 2002 (tracks with a circle at the genesis location, as illustrated in Fig. 18a). For these cases, the south-coast cyclones traveled northwards and approached eastern Hokkaido. Although the cyclogenesis occurred over or off the east coast of the main island of Japan, cyclones on January 12, 2022, April 27, 2013, and April 19, 1995, traveled north-eastward and approached eastern Hokkaido.

To understand why this case had the highest precipitation during the period of suitable temperatures for wet snow accretion, Figure 18b illustrates the tracks of the extratropical cyclones during the temperatures suitable for wet snow accretion at Monbetsu for each event. Most events had extratropical cyclones located off the southeast of eastern Hokkaido. This suggests that precipitation mainly originated from stratiform clouds ahead of the warm front of a cyclone. For the May 10, 1996, event, which had a longer duration than the case study by 10 h, the cyclone traveled eastward and away from Hokkaido during the latter part of the event, which suppressed precipitation amount. For the

December 31, 2008, event, which had the second longest duration among the 10 events, the cyclone over the southern edge of the Okhotsk Sea dissipated before the temperatures at Monbetsu reached the suitable range for wet snow accretion. Precipitation in the December 2008 event resulted from northerly cold surges over the Okhotsk Sea associated with an extratropical cyclone located over the Bering Sea. These results suggest that the extratropical cyclone remained southeast of eastern Hokkaido during the suitable temperature ranges for wet snow accretion at Monbetsu, resulting in the highest SAP value for this case. In addition, cyclone over the northern Japan Sea (C1 cyclone) may play a role for increasing precipitation. No cyclone was maintained over the northern Japan Sea in historical events.

7. Concluding remarks

Meteorological conditions that caused heavy wet snow accretion around the coastal area of the Okhotsk Sea on December 22–23, 2022, were investigated using a reanalysis dataset, station observations, and numerical simulations by employing the WRF. We focused on the three factors that cause wet snow accretion, i.e., strong winds, snowfall, and temperatures slightly above 0°C. An analysis of the snow accretion potential using AMeDAS showed that this period was the most favorable for the occurrence of wet snow accretion in Hokkaido since 1976. Multiple extratropical cyclones around Hokkaido contributed to snowfall and strong winds. Together with a stagnant extratropical cyclone over the northern Japan Sea (C1 cyclone), a northward-moving extratropical cyclone that landed in eastern Hokkaido (C2 cyclone) created large-scale cyclonic circulation in northern Japan. The coastal area of the Okhotsk Sea was in the northern part of cyclonic circulation, where narrow isobar intervals yielded strong easterly winds. A previous study indicated that a northward-moving extratropical cyclone caused strong winds in Hokkaido (Hirata 2021).

The cloud system, accompanied by the C2 cyclone, contributed to snowfall in the Monbetsu area. Snowflakes and ice crystals that fell from stratiform clouds north of the C2 cyclone (midnight on December 22) grew below an altitude of 4 km through the depositional growth of water vapor transported by the nearly saturated CCB of the C2 cyclone. These results indicate that synoptic-scale vapor transport involving multiple extratropical cyclones reinforced snowfall through the depositional growth of solid hydrometers. The temperature and humidity in the CCB control the amount of precipitation from stratiform clouds north of the warm front (Schultz 2001). In this case, the nearly saturated CCB with respect to liquid water reinforced snowfall.

The maintenance of temperatures slightly above 0 °C is crucial for the occurrence of wet snow accretion. A backward trajectory analysis revealed that the temperatures suitable for wet snow accretion were sustained by the cancellation of heating from sea surfaces and cooling from the melting of solid hydrometers. A sensitivity experiment showed that the temperature increased by 0.5–1 °C compared with that in the control experiment if cooling from the melting of solid hydrometer was excluded. No wet snow accretion on electrical wires occurred at temperatures above 1 °C in previous observational studies at Kushiro. This implies that cooling from melting snowflake is crucial for the occurrence of wet snow accretion. The current analysis suggests that both synoptic-scale phenomena, including strong winds and moisture transport associated with extratropical cyclones, and micro- and local-scale phenomena, including cloud microphysics, play important roles in the occurrence of heavy wet snow accretion.

The historical wet snow events at Monbetsu also have similar northward-moving cyclone tracks. However, precipitation amounts in historical events were less than those in this event because cyclones moved away from the southeastern area off of east Hokkaido.

Global warming modulates the occurrence of wet snow accretion (Tropea and Stewart 2021). In northern Hokkaido, including the coastal area of the Okhotsk Sea, wet snow is projected to increase in the future climate because the frequency of extratropical cyclones that move northward to Hokkaido is also projected to increase (Ohba and Sugimoto 2020). Further studies on the risk of disasters associated with heavy wet snow accretion in this area in the current and future climate are necessary for policy makers when designing countermeasures.

Data Availability Statements

The ERA5 reanalysis dataset was downloaded from the Climate Data Store (https://doi.org/10.24381/cds.bd0915c6). The AMeDAS dataset is available on the JMA website (https://www.data.jma.go.jp/risk/obsdl/index.php). The 100 m meshed land-use data were downloaded from the National Land Numerical Information Download Site operated by the Ministry of Land, Infrastructure, Transport and Tourism (https://nlftp.mlit.go.jp/ksj/gml/datalist/KsjTmplt-L03-b.html). The version 4.4.2 of the WRF model was downloaded from the GitHub repository (https://github.com/wrf-model/WRF). The LAGRANTO was downloaded from https://iacweb.ethz.ch/staff/sprenger/lagranto/home.html. The University of Melbourne cyclone detection and tracking algorithm was downloaded from https://cyclonetracker.earthsci.unimelb.edu.au/.

Acknowledgements

The authors thank Drs. Sachiho A. Adachi and Akira Kuwano-Yoshida and an anonymous reviewer for their constructive comments, which helped improve the manuscript.

Appendix

Table A1 summarizes the parameters used for the cyclone detection and tracking.

References

Admirat, P., 2008: *Wet Snow Accretion on Overhead Lines.*

Benjamin, S. G., G. A. Grell, J. M. Brown, T. G. Smirnova, and R. Bleck, 2004: Mesoscale Weather

Prediction with the RUC Hybrid Isentropic–Terrain-Following Coordinate Model. *Monthly Weather Review*, **132,** 473-494, 10.1175/1520-0493(2004)132<0473:Mwpwtr>2.0.Co;2.

Bonelli, P., M. Lacavalla, P. Marcacci, G. Mariani, and G. Stella, 2011: Wet snow hazard for power lines: a forecast and alert system applied in Italy. *Nat Hazard Earth Sys*, **11,** 2419-2431, 10.5194/nhess-11-2419-2011.

Browning, K. A., 1986: Conceptual Models of Precipitation Systems. *Weather and Forecasting*, **1,** 23-41, 10.1175/1520-0434(1986)001<0023:Cmops>2.0.Co;2.

Cabinet Office, 2023: *White Paper on Disster Management 2023 (in Japanese).* Vol. 2023, Cabinet Office,https://www.bousai.go.jp/kaigirep/hakusho/pdf/r5_all.pdf.

Carlson, T. N., 1980: Airflow Through Midlatitude Cyclones and the Comma Cloud Pattern. *Monthly Weather Review*, **108,** 1498-1509, 10.1175/1520-0493(1980)108<1498:Atmcat>2.0.Co;2.

CIGRE, 2006: *Guidelines for Meteorological Icing Models, Statistical Methods and Topographical Effects.* Cigré Working Group B2.16, TB 291, 116 pp.

Dalle, B., and P. Admirat, 2011: Wet snow accretion on overhead lines with French report of experience. *Cold Regions Science and Technology*, **65,** 43-51, 10.1016/j.coldregions.2010.04.015.

Ducloux, H., and B. E. Nygaard, 2014: 50-year return-period wet-snow load estimation based on weather station data for overhead line design in France. *Nat Hazard Earth Sys*, **14,** 3031-3041, 10.5194/nhess-14-3031-2014.

Farzaneh, M., 2008: *Atmospheric Icing of Power Networks.* 1 ed. Springer, 381 pp.

Frick, C., and H. Wernli, 2012: A Case Study of High-Impact Wet Snowfall in Northwest Germany (25–27 November 2005): Observations, Dynamics, and Forecast Performance. *Weather and Forecasting*, **27,** 1217-1234, 10.1175/waf-d-11-00084.1.

Frick, C., A. Seifert, and H. Wernli, 2013: A bulk parametrization of melting snowflakes with explicit liquid water fraction for the COSMO model. *Geoscientific Model Development*, **6,** 1925-1939, 10.5194/gmd-6-1925-2013.

Gómez-Navarro, J. J., C. C. Raible, and S. Dierer, 2015: Sensitivity of the WRF model to PBL parametrisations and nesting techniques: evaluation of wind storms over complex terrain. *Geoscientific Model Development*, **8,** 3349-3363, 10.5194/gmd-8-3349-2015.

Hanesiak, J., and Coauthors, 2022: The Severe Multi-Day October 2019 Snow Storm Over Southern Manitoba, Canada. *Atmosphere-Ocean*, **60,** 65-87, 10.1080/07055900.2022.2060794.

Hasemi, T., and K. Baba, 1994: On the genesis of local fronts and snow accretion in the Kanto Plain accompanied by cyclones passing along the south of Honshu island. *Journal of the Japanese Society of Snow and Ice*, **56,** 119-126, 10.5331/seppyo.56.119.

Hersbach, H., and Coauthors, 2020: The ERA5 global reanalysis. *Quarterly Journal of the Royal Meteorological Society*, **146,** 1999-2049, 10.1002/qj.3803.

Hirata, H., 2021: Climatological Features of Strong Winds Caused by Extratropical Cyclones around Japan. *Journal of Climate*, **34,** 4481-4494, 10.1175/jcli-d-20-0577.1.

Hobbs, P. V., and J. D. Locatelli, 1978: Rainbands, Precipitation Cores and Generating Cells in a Cyclonic Storm. *Journal of the Atmospheric Sciences*, **35,** 230-241, 10.1175/1520-0469(1978)035<0230:Rpcagc>2.0.Co;2.

Houze, R. A., P. V. Hobbs, K. R. Biswas, and W. M. Davis, 1976: Mesoscale Rainbands in Extratropical Cyclones. *Monthly Weather Review*, **104,** 868-878, 10.1175/1520-0493(1976)104<0868:Mriec>2.0.Co;2.

Iacono, M. J., J. S. Delamere, E. J. Mlawer, M. W. Shephard, S. A. Clough, and W. D. Collins, 2008: Radiative forcing by long-lived greenhouse gases: Calculations with the AER radiative transfer models. *Journal of Geophysical Research*, **113**, 10.1029/2008jd009944.

Janjić, Z. I., 1990: The Step-Mountain Coordinate: Physical Package. *Monthly Weather Review*, **118,** 1429-1443, 10.1175/1520-0493(1990)118<1429:Tsmcpp>2.0.Co;2.

——, 1994: The Step-Mountain Eta Coordinate Model: Further Developments of the Convection, Viscous Sublayer, and Turbulence Closure Schemes. *Monthly Weather Review*, **122,** 927-945, 10.1175/1520-0493(1994)122<0927:Tsmecm>2.0.Co;2.

Kawazoe, S., M. Inatsu, T. J. Yamada, and T. Hoshino, 2020: Climate Change Impacts on Heavy Snowfall in Sapporo Using 5-km Mesh Large Ensemble Simulations. *Sola*, **16,** 233-239, 10.2151/sola.2020-039.

Kondo, J., and H. Yamazawa, 1986: Aerodynamic roughness over an inhomogeneous ground surface. *Boundary-Layer Meteorology*, **35,** 331-348, 10.1007/bf00118563.

Locatelli, J. D., and P. V. Hobbs, 1974: Fall speeds and masses of solid precipitation particles. *Journal of Geophysical Research*, **79,** 2185-2197, 10.1029/JC079i015p02185.

Madonna, E., H. Wernli, H. Joos, and O. Martius, 2014: Warm Conveyor Belts in the ERA-Interim Dataset (1979–2010). Part I: Climatology and Potential Vorticity Evolution. *Journal of Climate*, **27,** 3-26, 10.1175/jcli-d-12-00720.1.

Makkonen, L., 1989: Estimation of wet snow accretion on structures. *Cold Regions Science and Technology*, **17,** 83-88, 10.1016/s0165-232x(89)80018-7.

Matsuo, T., Y. Sasyo, and Y. Sato, 1981: Relationship between Types of Precipitation on the Ground and Surface Meteorological Elements. *Journal of the Meteorological Society of Japan. Ser. II*, **59,** 462-476, 10.2151/jmsj1965.59.4_462.

Matsushita, H., and F. Nishio, 2006: Climatological characteristics corresponding to the occurrence of precipitation resulting in snow accretion in Japan. *Journal of the Japanese Society of Snow and Ice*, **68,** 421-432, 10.5331/seppyo.68.421.

Milbrandt, J. A., and H. Morrison, 2016: Parameterization of Cloud Microphysics Based on the Prediction of Bulk Ice Particle Properties. Part III: Introduction of Multiple Free Categories. *Journal of the Atmospheric Sciences*, **73,** 975-995, 10.1175/jas-d-15-0204.1.

Mitra, S. K., O. Vohl, M. Ahr, and H. R. Pruppacher, 1990: A Wind Tunnel and Theoretical Study of the Melting Behavior of Atmospheric Ice Particles. IV: Experiment and Theory for Snow Flakes. *Journal of the Atmospheric Sciences*, **47,** 584-591, 10.1175/1520-

0469(1990)047<0584:Awtats>2.0.Co;2.

Morrison, H., and J. A. Milbrandt, 2015: Parameterization of Cloud Microphysics Based on the Prediction of Bulk Ice Particle Properties. Part I: Scheme Description and Idealized Tests. *Journal of the Atmospheric Sciences*, **72,** 287-311, 10.1175/jas-d-14-0065.1.

Murray, J. R., and I. Simmonds, 1991a: A numerical scheme for tracking cyclone centres from digital data Part I: development and operation of the scheme. *Australian Meteorological Magazine*, **39,** 155-166

——, 1991b: A numerical scheme for tracking cyclone centres from digital data Part II: application to January and July general circulation model simulatins. *Australian Meteorological Magazine*, **39,** 167-180

Neiman, P. J., M. A. Shapiro, and L. S. Fedor, 1993: The Life Cycle of an Extratropical Marine Cyclone. Part II: Mesoscale Structure and Diagnostics. *Monthly Weather Review*, **121,** 2177-2199, 10.1175/1520-0493(1993)121<2177:Tlcoae>2.0.Co;2.

Nishihara, T., K. Ueno, H. Ichikawa, H. Matsumiya, and S. Sugimoto, 2017: Field observation of wet snow accretion using short dummy conductor supported by wire ropes - Verification of estimation methods of snow accretion and performance of anti-snow-accretion devices -. CRIEPI Research Report, N16002.

Nygaard, B. E. K., H. Ágústsson, and K. Somfalvi-Tóth, 2013: Modeling Wet Snow Accretion on Power Lines: Improvements to Previous Methods Using 50 Years of Observations. *Journal of*

Applied Meteorology and Climatology, **52,** 2189-2203, 10.1175/jamc-d-12-0332.1.

Ohara, S., and Coauthors, 2017: Numerical and observational studies on meteorological condition of salt snow damage to insulators- A proposal of indicator of possibility of salt snow damage to insulators with wet and packed snow accretion -. CRIEPI Research Report, V17001.

Ohba, M., and S. Sugimoto, 2020: Impacts of climate change on heavy wet snowfall in Japan. *Climate Dynamics*, **54,** 3151-3164, 10.1007/s00382-020-05163-z.

Sakamoto, Y., 2000: Snow accretion on overhead wires. *Philosophical Transactions of the Royal Society of London. Series A: Mathematical, Physical and Engineering Sciences*, **358,** 2941-2970, 10.1098/rsta.2000.0691.

Schultz, D. M., 2001: Reexamining the Cold Conveyor Belt. *Monthly Weather Review*, **129,** 2205-2225, 10.1175/1520-0493(2001)129<2205:Rtccb>2.0.Co;2.

Shimada, S., T. Ohsawa, S. Chikaoka, and K. Kozai, 2011: Accuracy of the Wind Speed Profile in the Lower PBL as Simulated by the WRF Model. *Sola*, **7,** 109-112, 10.2151/sola.2011-028.

Shimizu, M., H. Matsumiya, S. Sugimoto, T. Ishikawa, A. Hashimoto, T. Nishihara, and H. Hirakuchi, 2017: Report on 10 years research of snow damage of overhead transmission facilities (Part I) -Development of practical measures on heavily accreted snow and galloping-. CRIEPI Research Report, N16010.

Skamarock, W. C., and Coauthors, 2021: A DESCRIPTION OF THE ADVANCED RESEARCH WRF MODEL VERSION 4.3. NCAR Tech. Note, 145 pp.

Sprenger, M., and H. Wernli, 2015: The LAGRANTO Lagrangian analysis tool – version 2.0. *Geoscientific Model Development*, **8,** 2569-2586, 10.5194/gmd-8-2569-2015.

Takeuchi, M., 1978: Snow Accretion on Traffic-Control Signs and Its Prevention. *Journal of the Japanese Society of Snow and Ice*, **40,** 117-127, 10.5331/seppyo.40.117.

Tropea, B., and R. Stewart, 2021: Assessing past and future hazardous freezing rain and wet snow events in Manitoba, Canada using a pseudo-global warming approach. *Atmospheric Research*, **259**, 10.1016/j.atmosres.2021.105656.

Tsopouridis, L., C. Spensberger, and T. Spengler, 2020: Cyclone intensification in the Kuroshio region and its relation to the sea surface temperature front and upper-level forcing. *Quarterly Journal of the Royal Meteorological Society*, 10.1002/qj.3929.

Wakahama, G., D. Kuroiwa, and K. Gotō, 1977: Snow Accretion on Electric Wires and its Prevention. *Journal of Glaciology*, **19,** 479-487, 10.3189/s0022143000215682.

Yoshida, A., and Y. Asuma, 2004: Structures and Environment of Explosively Developing Extratropical Cyclones in the Northwestern Pacific Region. *Monthly Weather Review*, **132,** 1121-1142, 10.1175/1520-0493(2004)132<1121:saeoed>2.0.co;2.

Zheng, Y., K. Alapaty, J. A. Herwehe, A. D. Del Genio, and D. Niyogi, 2016: Improving High-Resolution Weather Forecasts Using the Weather Research and Forecasting (WRF) Model with an Updated Kain–Fritsch Scheme. *Monthly Weather Review*, **144,** 833-860, 10.1175/mwr-d-15-0005.1.

List of Tables

List of **Figures**

Figure 1. Topography and geographic landmarks in the study area. The four map points represent the following locations: (1) Omu, (2) Monbetsu, (3) Nakashibetsu, and (4) Kushiro.

Figure 2. Geographic location of the model domains. Shading represents the terrain height in meters. The grid spacings are 5 and 1.667 km for D01 and D02, respectively.

Figure 3. Spatial patterns of the sea level pressure (black contours) and 10-m wind speed (shading) from the ERA5 reanalysis dataset, at 12-h intervals from 09 JST on December 22 to 21 JST on December 23, 2022. Contour intervals are 4 hPa. The cross marks represent the location of cyclones labeled C1 to C4. The warm and cold fronts are drawn manually based on equivalent potential temperature fields at 950 hPa. In (d), the purple line illustrates the track of the C2 cyclone.

Figure 4. Shaded spatial patterns of the horizontal wind divergence at 300 hPa and temperature at 850 hPa from the ERA5 reanalysis dataset at 12-h intervals from 09 JST on December 22 to 21 JST on December 23, 2022. Contours in the left column represent geopotential height at 500 hPa at intervals of 100 gpm and vectors in the right column represent horizontal wind (vector) at 850 hPa

Figure 5. Station observations of various parameters derived from the AMeDAS over Hokkaido. The parameters are (a) 24-h accumulated precipitation, (b) maximum wind speed at 10-m height, (c) mean temperature from 15 JST on December 22 to 15 JST on December 23, 2022, and (d) 24-h accumulated snow accretion potential.

Figure 6. Observed time-series at Monbetsu Station from the AMeDAS. Plots of the (a)

temperature, (b) sunshine duration, (c) precipitation rate, (d) snowfall rate, (e) snow depth, (f) wind speed, and (g) wind barbs (full and half bars denote 1 and 5 m s^{-1} and flags represent 10 m s^{-1}) on December 22–23, 2022. The colors in (g) represent observed weather types.

Figure 7. Comparisons of the time-series at Monbetsu Station between the AMeDAS observations and WRF simulations. Time-series of the (a) 10-m wind direction, (b) 10-m wind speed, (c) accumulated precipitation, (d) 2-m temperature, and (e) hourly SAP. Height correction is applied to the simulated temperature using the temperature lapse rate between the lowermost two model levels.

Figure 8. Simulated equivalent radar reflectivity at a height of 2,000 m ((a) 21 JST on December 22, 2022, and (b) 03 JST, (c) 10 JST, and (d) 13 JST on December 23, 2022). The solid white circles denote the location of Monbetsu Station.

Figure 9. Time-vertical cross-section of the simulated equivalent radar reflectivity at Monbetsu Station. Black solid contours present the potential temperature at intervals of 4 K, and the black dotted line is the melting level.

Figure 10. Simulated horizontal distributions and vertical cross-sections across Monbetsu Station at 00 JST on December 23, 2022. In (a), the shading, contours, and vectors represent temperature at 925 hPa, geopotential height at 925 hPa, and vertically integrated vapor flux, respectively. In (b), the shading and magenta dots represent the specific humidity at a height of 2,000 m and the location where the vertical velocity at a height of 2,000 m exceeds 1.5 m s^{-1}, respectively. Vertical cross-sections in (c) are along a black broken line in (a) and in (d)–(f) along a black broken line in (b). In (c), the shading,

contours, and arrows represent the water vapor mixing ratio, potential temperature at 10 K intervals, and horizontal wind, respectively. In (d), the shading and contours represent the equivalent radar reflectivity and potential temperature at 10 K intervals, respectively. In (e), the shading, black contour, and orange contours represent the mixing ratio of ice (sum of categories 1 and 2), melting level, and rain mixing ratio at intervals of 0.1 g kg^{-1}, respectively. In (f), the shading and black contours represent the riming fraction of ice category 1 and temperature at 10 °C intervals, respectively. Gray broken lines in (c)–(f) denote the location at Monbetsu Station.

Figure 11. Simulated vertical profiles of the tendency of free ice hydrometers (sum of categories 1 and 2) at Monbetsu Station at (a) 22 JST on December 22, (b) 03 JST on December 23, and (b) 13 JST on December 23, 2022.

Figure 12. Simulated vertical profiles of the potential temperature (θ), equivalent potential temperature (θ_e), saturated potential temperature with respect to liquid water ($\theta^{*}{}_{e}$), and vapor mixing ratio (Q_{vapor}) at Monbetsu at (a) 00 JST and (b)03 JST on 23 December 23, 2022.

Figure 13. Same as Fig. 10 except for at 03 JST on December 23, 2022.

Figure 14. Simulated horizontal distributions and vertical cross-sections across Monbetsu Station at 13 JST on December 23, 2022. In (a), the shading, contours, and vectors represent the temperature at 925 hPa, geopotential height at 925 hPa, and vertically integrated vapor flux, respectively. In (b), the shading and magenta dots represent the specific humidity at a height of 2,000 m and the location where the vertical velocity at a height of 2,000 m exceeds 1.5 m s^{-1}, respectively. Vertical cross-

sections in (c) are along a black broken line in (a) and in (d)–(f) along a black broken line in (b). In (c), the shading, contours, and arrows represent the water vapor mixing ratio, potential temperature at10 K intervals, and horizontal wind, respectively. In (d), the shading and contours represent the equivalent radar reflectivity and potential temperature at 10 K intervals, respectively. In (e), the shading, black contour, and orange contours represent the mixing ratio of ice (sum of categories 1 and 2), melting level, and rain mixing ratio at 0.1 g kg^{-1} intervals, respectively. In (f), the shading and black contours represent the riming fraction of ice category 1 and temperature at 10 °C intervals, respectively. Gray broken lines in (c)–(f) denote the location of Monbetsu Station.

Figure 15. Location and time-evolution along trajectories. On map (a), the height of the trajectories is shaded, and orange dots denote locations in a 3-h interval. Time-evolutions are the (b) height, (c) potential temperature, (d) temperature with SST (red), and (e) relative humidity. In (b)–(e), the light and dark color shadings represent the 5–95 and 25–75 percentile widths, and the black line denotes median values. The horizontal axis shows the time since the release of initial parcels (14 JST on December 23, 2022).

Figure 16. Time-evolution of the median heating rates from the (a) parameterization schemes and (b) microphysical processes along trajectories. The horizontal axis shows the time since the release of initial parcels (14 JST on December 23, 2022).

Figure 17. Time-series of the temperature at a 2-m height at Monbetsu Station from the control and no-melt-heating simulations and AMeDAS observation. Height correction is applied to the

simulated temperature using the temperature lapse rate between the lowermost two layers.

Figure 18. Surface cyclone tracks for the 10 highest SAP events at Monbetsu. In (a), tracks the closest to eastern Hokkaido are illustrated with the December 2022 case highlighted by the thick black line. (b) is identical to (a), except for tracks illustrated with broken lines with periods of suitable temperature for wet snow accretion (0–2 °C) as thick lines. The genesis points are indicated by a circle for tracks of five cyclones exhibiting a similar path to that of the present case in (a), and a square is used for two tracks that exhibit the longest duration (2008/12/31 and 1996/5/10) in (b).

Table 1. Simulation setup for the outer (D1) and inner domains (D2).

	D1	D2
Initial and Boundary condition data	ERA5	Result of D1
Initial time [JST]	12/22/2022 06:00	12/22/2022 09:00
End time [JST]	12/23/2022 18:00	
Time step	25 s	8.33 s
Output interval	60 min	15 min
Grid points	720×540	1555×1102
Vertical layers	45	
Vertical grid spacing	Stretching grid: approximately 50 m at the bottom and approximately 550 m at the model top.	
Horizontal resolution	5 km	1.667 km
PBL physics	Mellor-Yamada-Janjic TKE scheme (Janjić 1994)	
Surface layer	Monin-Obukhov (Janjic Eta) similarity (Janjić 1990)	
Land surface	RUC Land-Surface Model (Benjamin et al., 2004)	
Cloud microphysics	P3 (Morrison and Milbrandt 2015)	
Cumulus scheme	Multi-scale Kain-Fritsch (Zheng et al., 2016)	–
Short wave radiation	RRTMG (Iacono et al., 2008)	
Long wave radiation	RRTMG (Iacono et al., 2008)	

Table 2. Bias and RMSE of the meteorological parameters at Monbetsu between 18 JST on December 22 and 15 JST on December 23.

	BIAS	RMSE
Temperature [°C]	-0.01	0.37
Wind speed [m s^{-1}]	2.00	3.65
Precipitation rate [mm h^{-1}]	-0.11	1.30
Hourly SAP [kg m^{-1} h^{-1}]	-2.15	11.9

Table 3. List of the 10 highest SAP events at Monbetsu.

Ranking	**Initial Time (Y/M/D-JST)**	**SAP [kg m^{-2}]**	**Duration [h]**	**Precipitation amount [mm]**	**Max. wind speed[1] [m s^{-1}]**
1	2022/12/22-21	429.7	22	85.9	9.5
2	2000/4/28-2	312.4	22	71.0	8.2
3	2000/4/11-16	298.5	12	43.7	11.0
4	2008/12/31-8	280.4	31	51.3	9.1
5	1996/5/10-4	250.5	32	66.4	9.2
6	2007/1/7-7	237.7	11	22.1	17.8
7	2002/11/27-1	196.5	9	51.4	7.3
8	2013/4/27-16	169.6	13	37.0	7.8
9	2022/1/12-9	146.9	17	26.3	9.8
10	1995/4/19-18	142.4	15	21.5	11.9

1: Maximum of 10 min-averaged wind speed.

Table A1. Parameters and values used for the cyclone detection and tracking algorithm.

Cyclone detection					
ni, nj	301, 301	drmx1	0.7	fccmn	0.
rproj	150.	drmx2	0.3	cvarad	0.75
rdiff	2.0	itmx1, itmx2	10	nrrdir	18
rdifz	2.0	diflt1, diflt2	1.0	rdincr	0.25
iopmxc	1	cmnh, cmnc	0.0	sphtrg	.false.
istmxc	11	cmnc1	0.5	rdpgrd	5.0
nshell	12	cmnc2	1.3	npgdir	12
mscrn	2	dpmn	0.1	ftopeq	0.005
sdrmx	10	zsmax	3000	cmncw	2.0
Tracking					
irevmx	400	refdt	0.25	qmxnew	0.75
wsteer	0.6	wpten	0.3	qmxopn	0.75
fsteer	2.0	wmotn	1.0	qmxwek	0.5
asteer	0.5	rcprob	12.0	rpbell	0.5

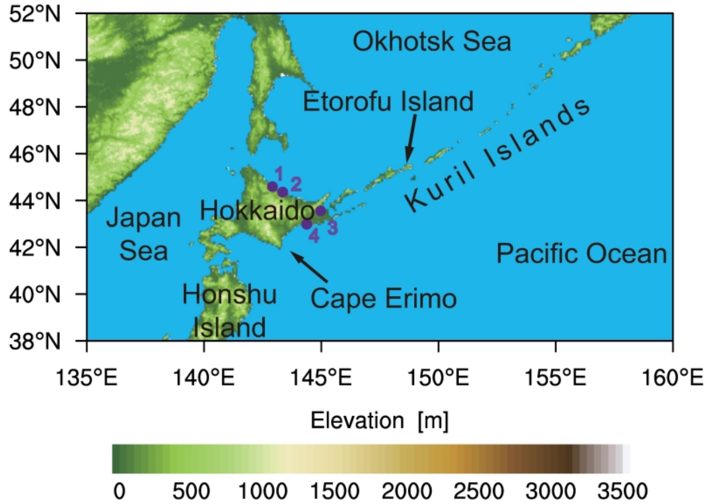

Figure 1. Topography and geographic landmarks in the study area. The four map points represent the following locations: (1) Omu, (2) Monbetsu, (3) Nakashibetsu, and (4) Kushiro.

227x190mm (600 x 600 DPI)

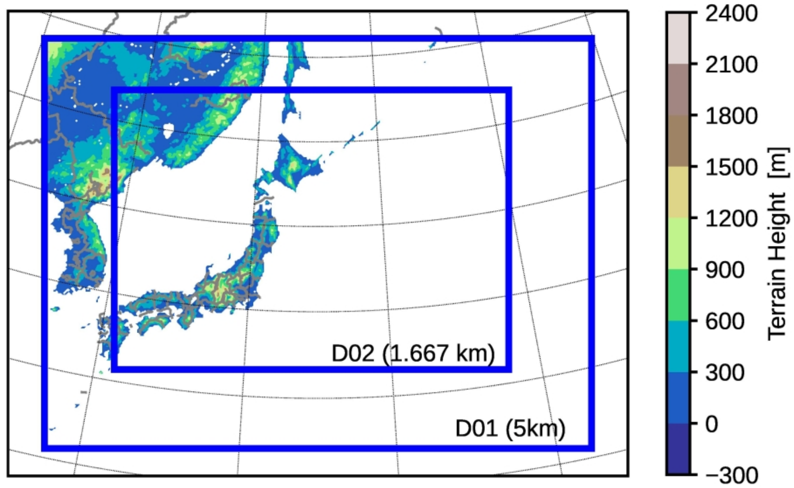

Figure 2. Geographic location of the model domains. Shading represents the terrain height in meters. The grid spacings are 5 and 1.667 km for D01 and D02, respectively.

162x121mm (600 x 600 DPI)

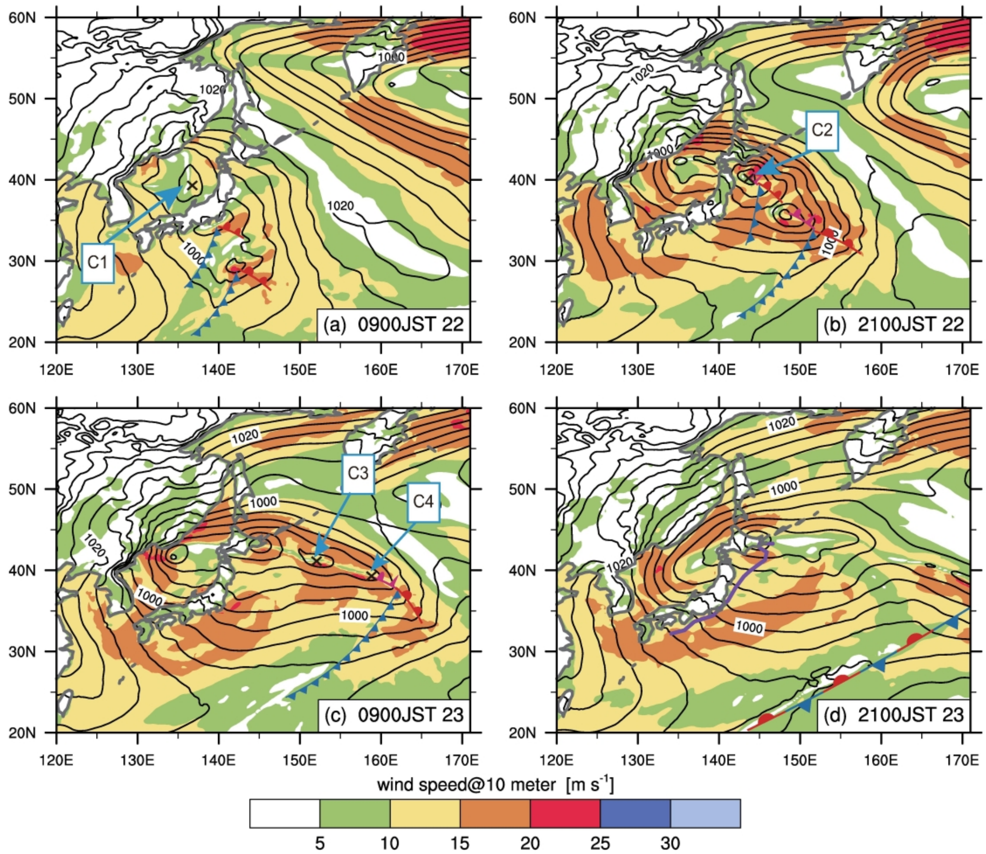

Figure 3. Spatial patterns of the sea level pressure (black contours) and 10-m wind speed (shading) from the ERA5 reanalysis dataset, at 12-h intervals from 09 JST on December 22 to 21 JST on December 23, 2022. Contour intervals are 4 hPa. The cross marks represent the location of cyclones labeled C1 to C4. The warm and cold fronts are drawn manually based on equivalent potential temperature fields at 950 hPa. In (d), the purple line illustrates the track of the C2 cyclone.

190x190mm (600 x 600 DPI)

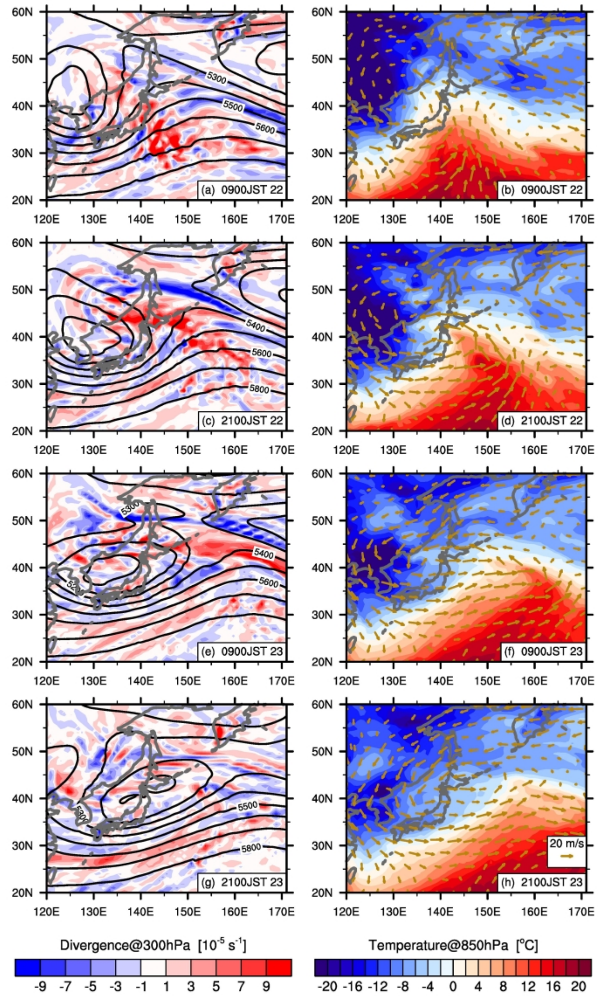

Figure 4. Shaded spatial patterns of the horizontal wind divergence at 300 hPa and temperature at 850 hPa from the ERA5 reanalysis dataset at 12-h intervals from 09 JST on December 22 to 21 JST on December 23, 2022. Contours in the left column represent geopotential height at 500 hPa at intervals of 100 gpm and vectors in the right column represent horizontal wind (vector) at 850 hPa.

190x190mm (600 x 600 DPI)

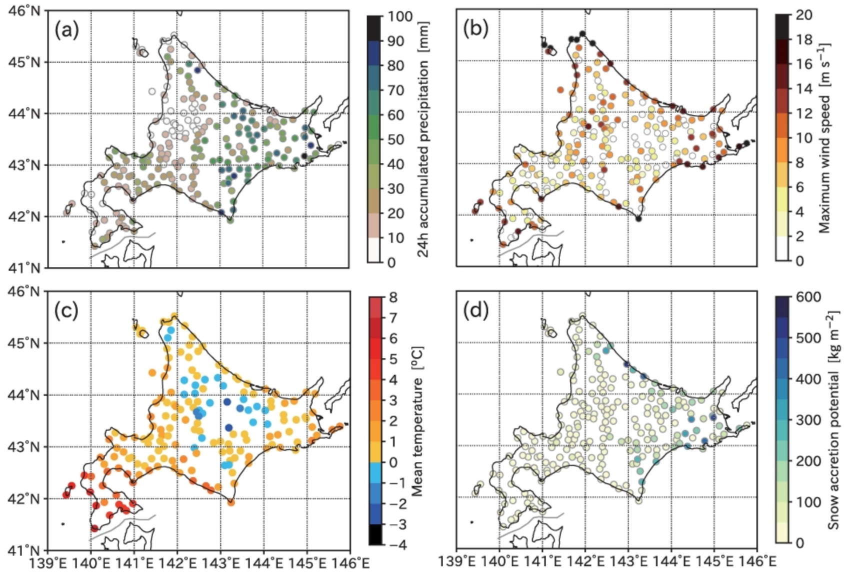

Figure 5. Station observations of various parameters derived from the AMeDAS over Hokkaido. The parameters are (a) 24-h accumulated precipitation, (b) maximum wind speed at 10-m height, (c) mean temperature from 15 JST on December 22 to 15 JST on December 23, 2022, and (d) 24-h accumulated snow accretion potential.

196x114mm (600 x 600 DPI)

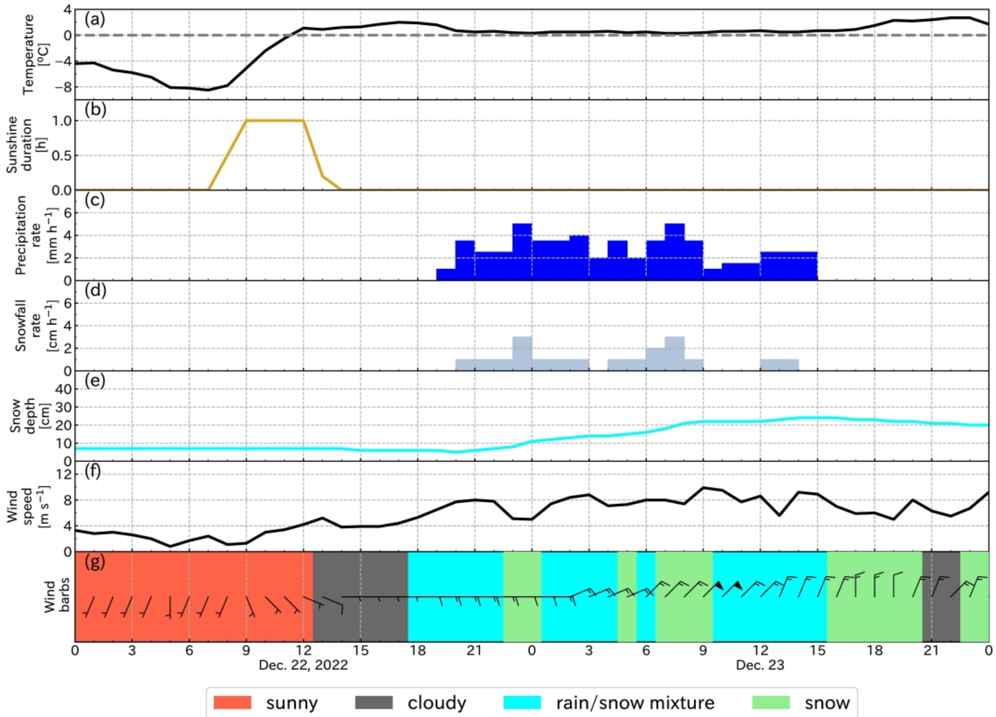

Figure 6. Observed time-series at Monbetsu Station from the AMeDAS. Plots of the (a) temperature, (b) sunshine duration, (c) precipitation rate, (d) snowfall rate, (e) snow depth, (f) wind speed, and (g) wind barbs (full and half bars denote 1 and 5 m s^{-1} and flags represent 10 m s^{-1}) on December 22–23, 2022. The colors in (g) represent observed weather types.

396x288mm (600 x 600 DPI)

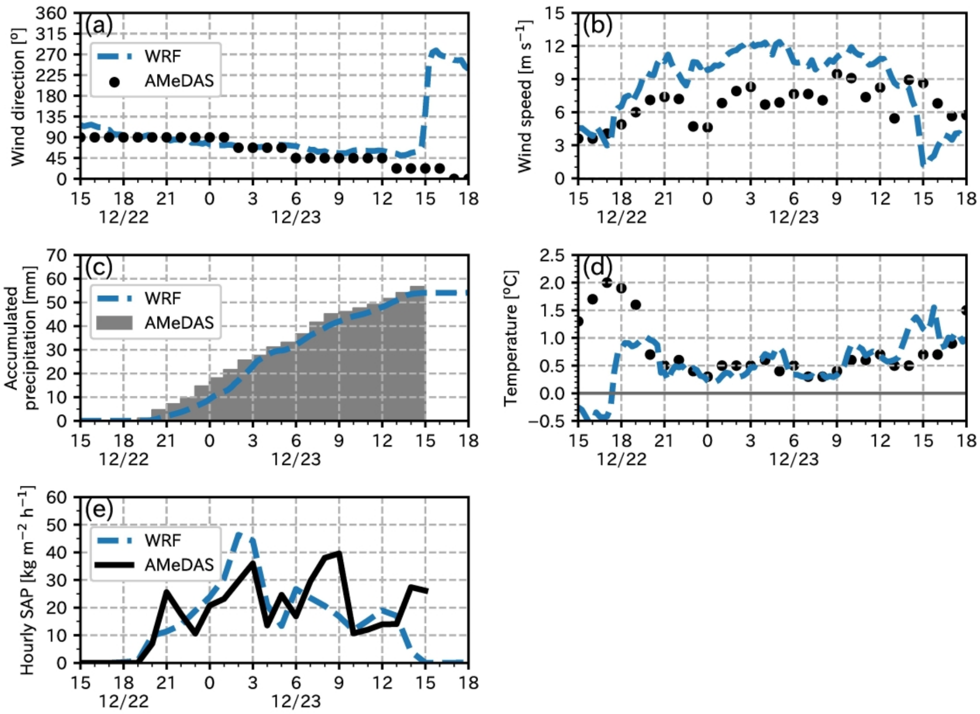

Figure 7. Comparisons of the time-series at Monbetsu Station between the AMeDAS observations and WRF simulations. Time-series of the (a) 10-m wind direction, (b) 10-m wind speed, (c) accumulated precipitation, (d) 2-m temperature, and (e) hourly SAP. Height correction is applied to the simulated temperature using the temperature lapse rate between the lowermost two model levels.

187x137mm (600 x 600 DPI)

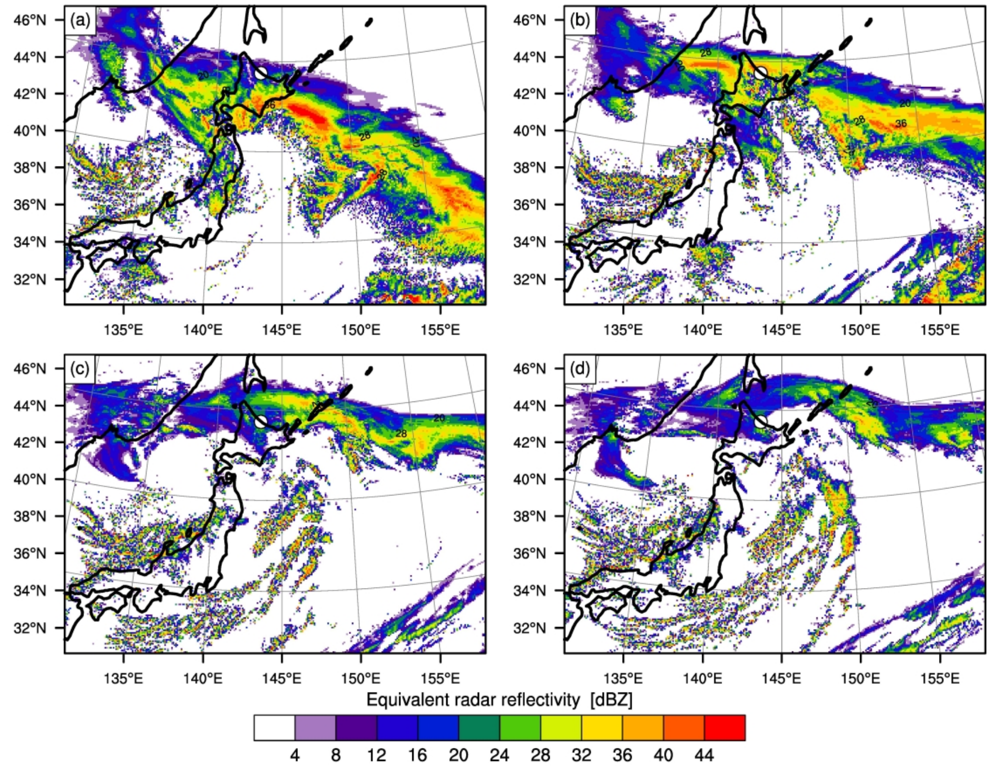

Figure 8. Simulated equivalent radar reflectivity at a height of 2,000 m ((a) 21 JST on December 22, 2022, and (b) 03 JST, (c) 10 JST, and (d) 13 JST on December 23, 2022). The solid white circles denote the location of Monbetsu Station.

190x190mm (600 x 600 DPI)

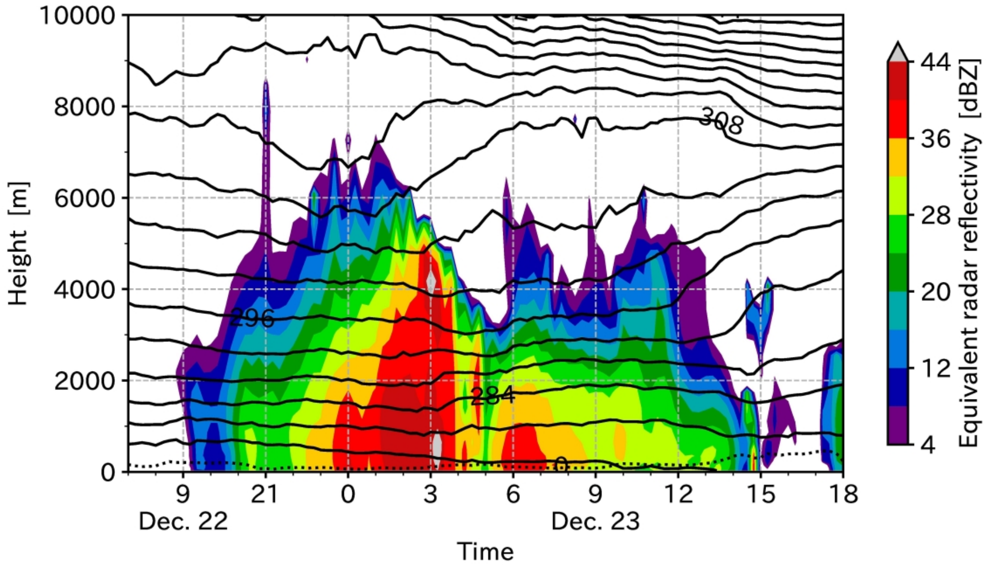

Figure 9. Time-vertical cross-section of the simulated equivalent radar reflectivity at Monbetsu Station. Black solid contours present the potential temperature at intervals of 4 K, and the black dotted line is the melting level.

199x116mm (600 x 600 DPI)

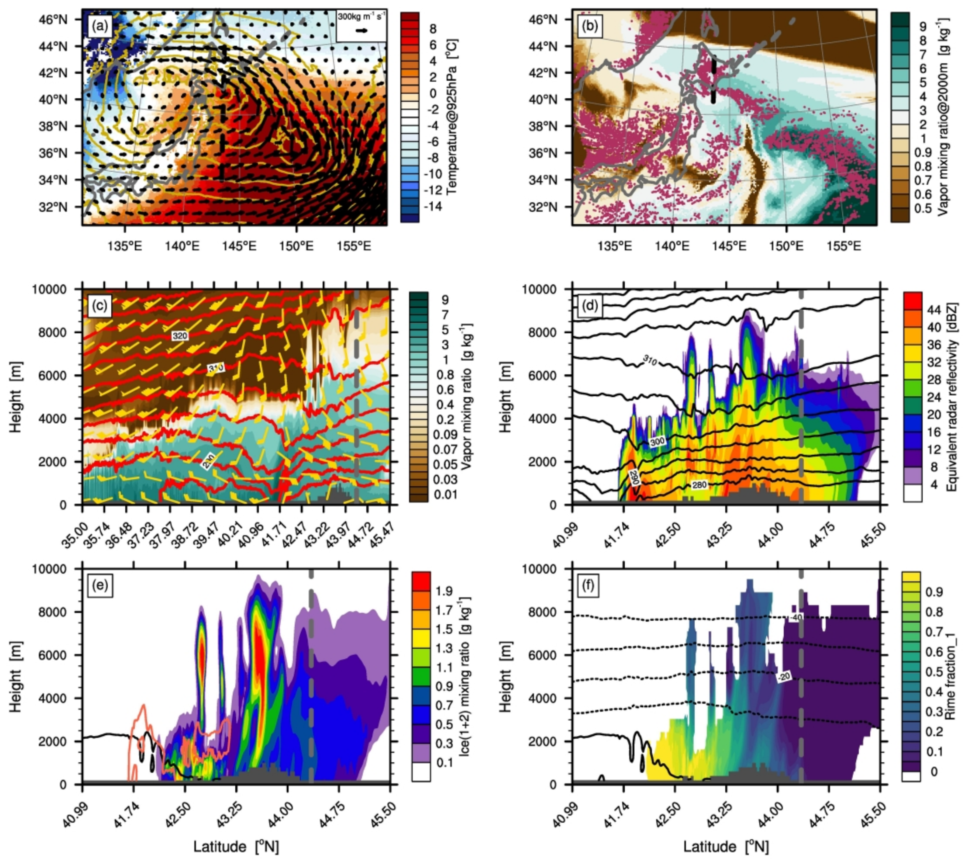

Figure 10. Simulated horizontal distributions and vertical cross-sections across Monbetsu Station at 00 JST on December 23, 2022. In (a), the shading, contours, and vectors represent temperature at 925 hPa, geopotential height at 925 hPa, and vertically integrated vapor flux, respectively. In (b), the shading and magenta dots represent the specific humidity at a height of 2,000 m and the location where the vertical velocity at a height of 2,000 m exceeds 1.5 m s^{-1}, respectively. Vertical cross-sections in (c) are along a black broken line in (a) and in (d)–(f) along a black broken line in (b). In (c), the shading, contours, and arrows represent the water vapor mixing ratio, potential temperature at 10 K intervals, and horizontal wind, respectively. In (d), the shading and contours represent the equivalent radar reflectivity and potential temperature at 10 K intervals, respectively. In (e), the shading, black contour, and orange contours represent the mixing ratio of ice (sum of categories 1 and 2), melting level, and rain mixing ratio at intervals of 0.1 g kg^{-1}, respectively. In (f), the shading and black contours represent the riming fraction of ice category 1 and temperature at 10 °C intervals, respectively. Gray broken lines in (c)–(f) denote the location at Monbetsu Station.

190x190mm (600 x 600 DPI)

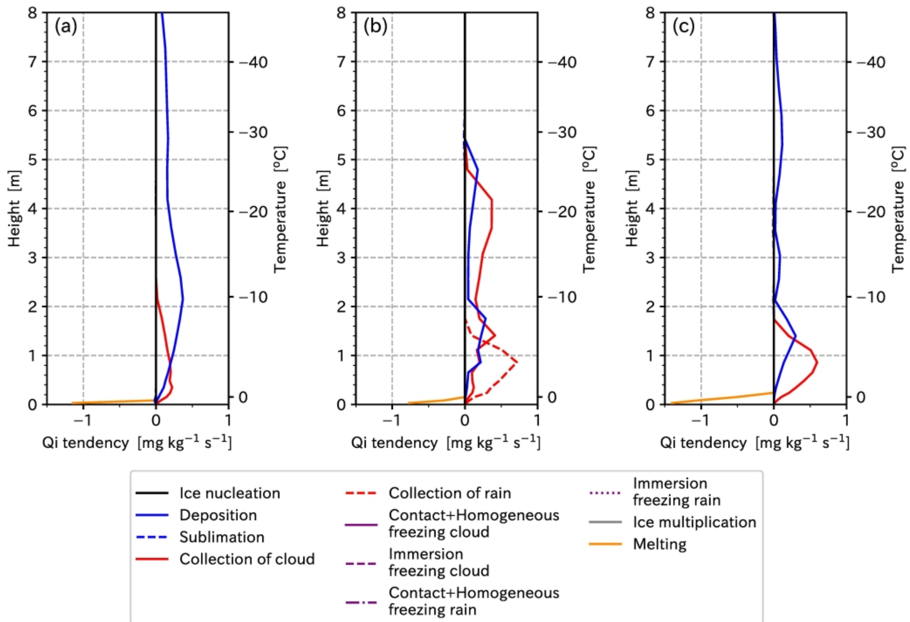

Figure 11. Simulated vertical profiles of the tendency of free ice hydrometers (sum of categories 1 and 2) at Monbetsu Station at (a) 00 JST, (b) 03 JST, and (b) 13 JST on December 23, 2022.

254x177mm (600 x 600 DPI)

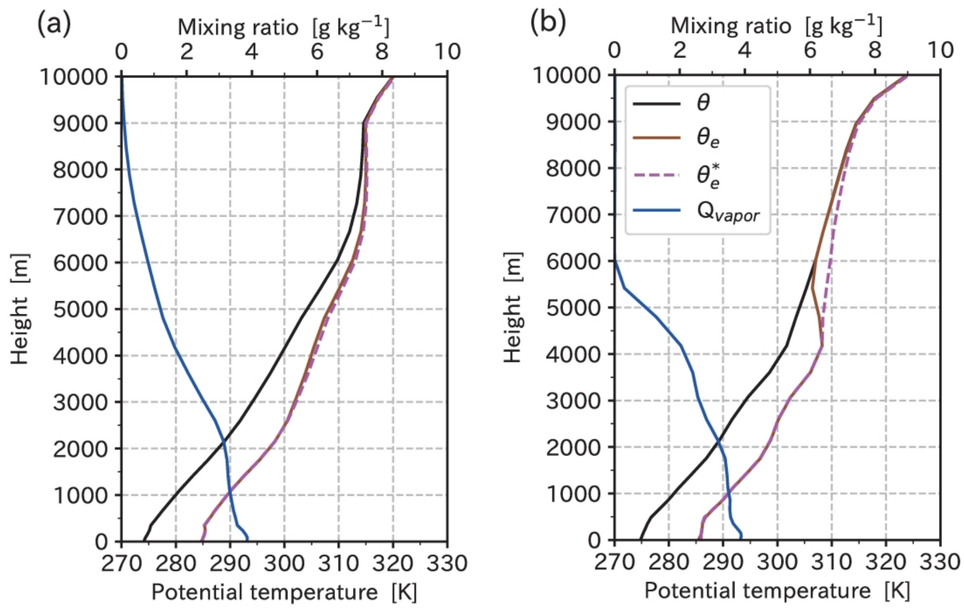

Figure 12. Simulated vertical profiles of the potential temperature (θ), equivalent potential temperature (θ_e), saturated potential temperature with respect to liquid water ($\theta^*{}_e$), and vapor mixing ratio (Qvapor) at Monbetsu at (a) 00 JST and (b)03 JST on 23 December 23, 2022.

190x122mm (600 x 600 DPI)

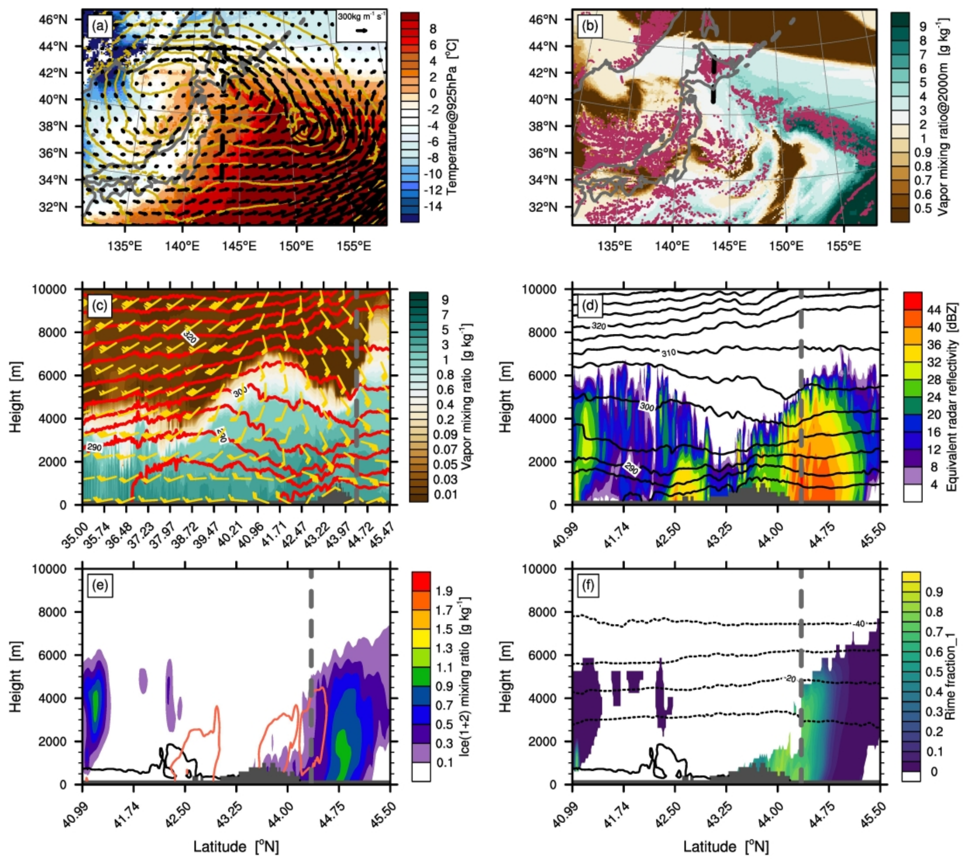

Figure 13. Same as Fig. 10 except for at 03 JST on December 23, 2022.

190x190mm (600 x 600 DPI)

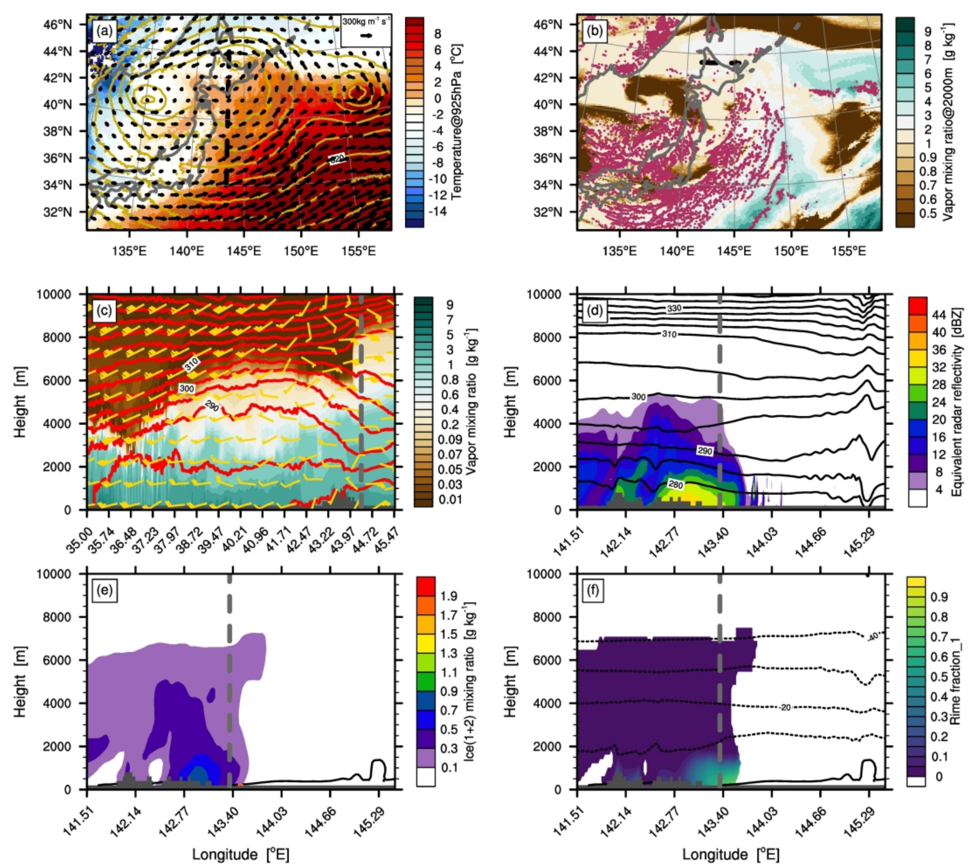

Figure 14. Simulated horizontal distributions and vertical cross-sections across Monbetsu Station at 13 JST on December 23, 2022. In (a), the shading, contours, and vectors represent the temperature at 925 hPa, geopotential height at 925 hPa, and vertically integrated vapor flux, respectively. In (b), the shading and magenta dots represent the specific humidity at a height of 2,000 m and the location where the vertical velocity at a height of 2,000 m exceeds 1.5 m s^{-1}, respectively. Vertical cross-sections in (c) are along a black broken line in (a) and in (d)–(f) along a black broken line in (b). In (c), the shading, contours, and arrows represent the water vapor mixing ratio, potential temperature at10 K intervals, and horizontal wind, respectively. In (d), the shading and contours represent the equivalent radar reflectivity and potential temperature at 10 K intervals, respectively. In (e), the shading, black contour, and orange contours represent the mixing ratio of ice (sum of categories 1 and 2), melting level, and rain mixing ratio at 0.1 g kg^{-1} intervals, respectively. In (f), the shading and black contours represent the riming fraction of ice category 1 and temperature at 10 °C intervals, respectively. Gray broken lines in (c)–(f) denote the location of Monbetsu Station.

190x190mm (600 x 600 DPI)

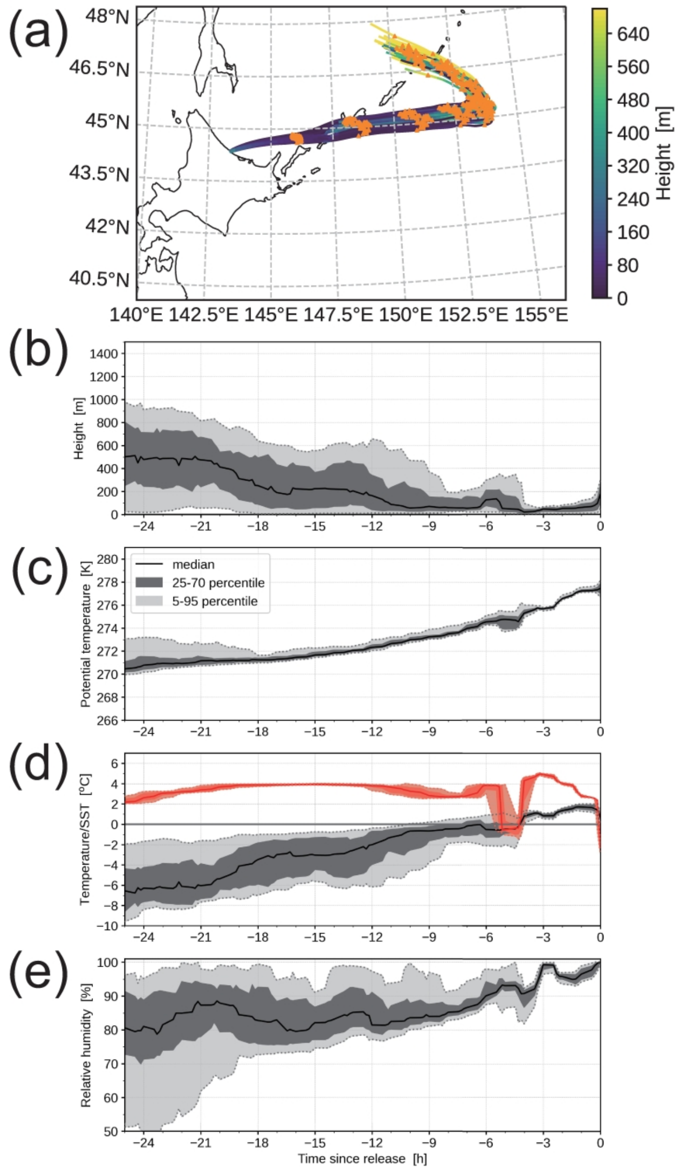

Figure 15. Location and time-evolution along trajectories. On map (a), the height of the trajectories is shaded, and orange dots denote locations in a 3-h interval. Time-evolutions are the (b) height, (c) potential temperature, (d) temperature with SST (red), and (e) relative humidity. In (b)–(e), the light and dark color shadings represent the 5–95 and 25–75 percentile widths, and the black line denotes median values. The horizontal axis shows the time since the release of initial parcels (14 JST on December 23, 2022).

189x299mm (600 x 600 DPI)

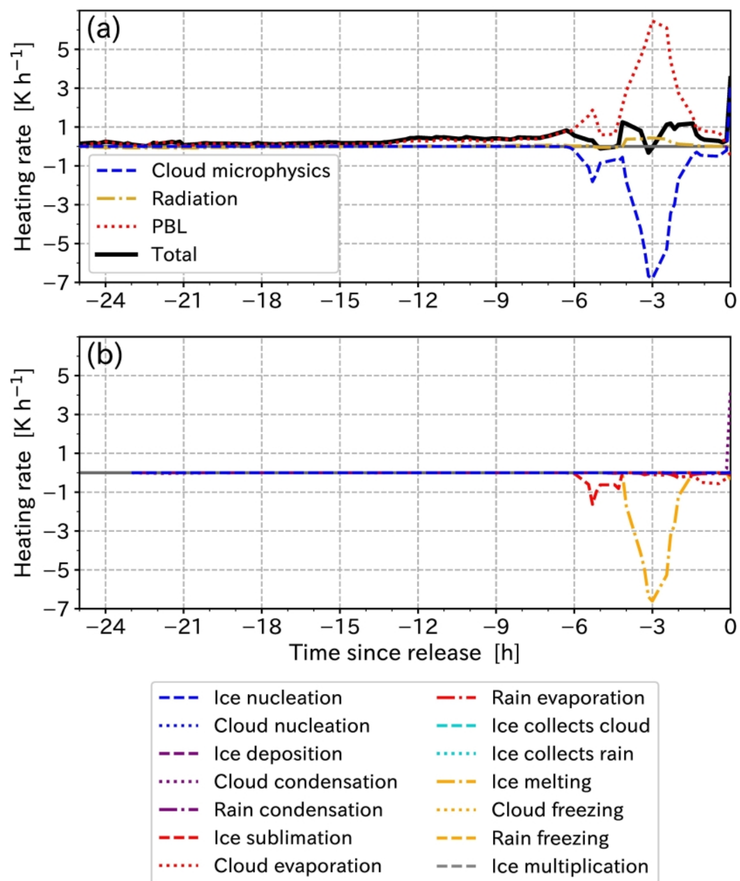

Figure 16. Time-evolution of the median heating rates from the (a) parameterization schemes and (b) microphysical processes along trajectories. The horizontal axis shows the time since the release of initial parcels (14 JST on December 23, 2022).

213x304mm (300 x 300 DPI)

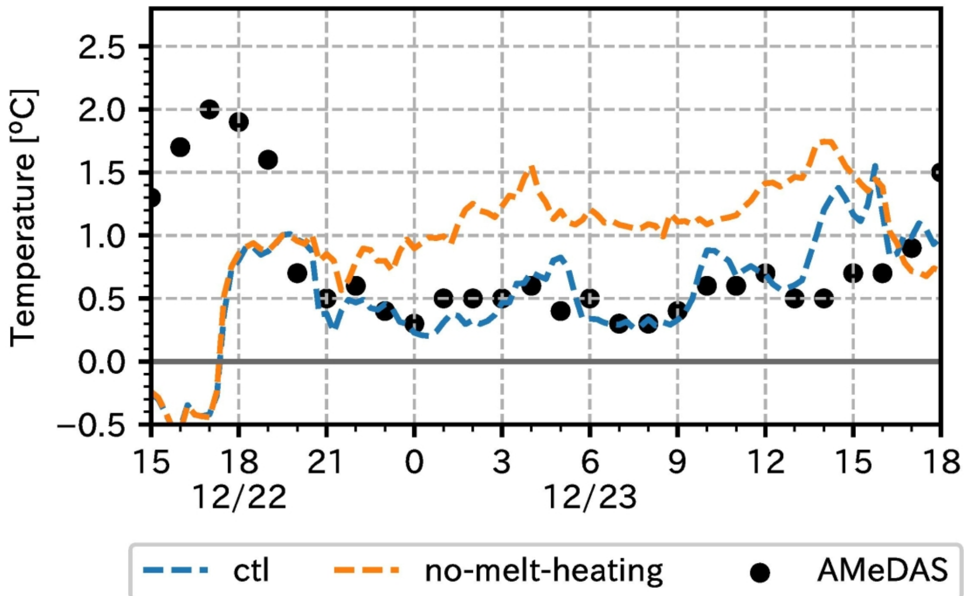

Figure 17. Time-series of the temperature at a 2-m height at Monbetsu Station from the control and no-melt-heating simulations and AMeDAS observation. Height correction is applied to the simulated temperature using the temperature lapse rate between the lowermost two layers.

99x63mm (600 x 600 DPI)

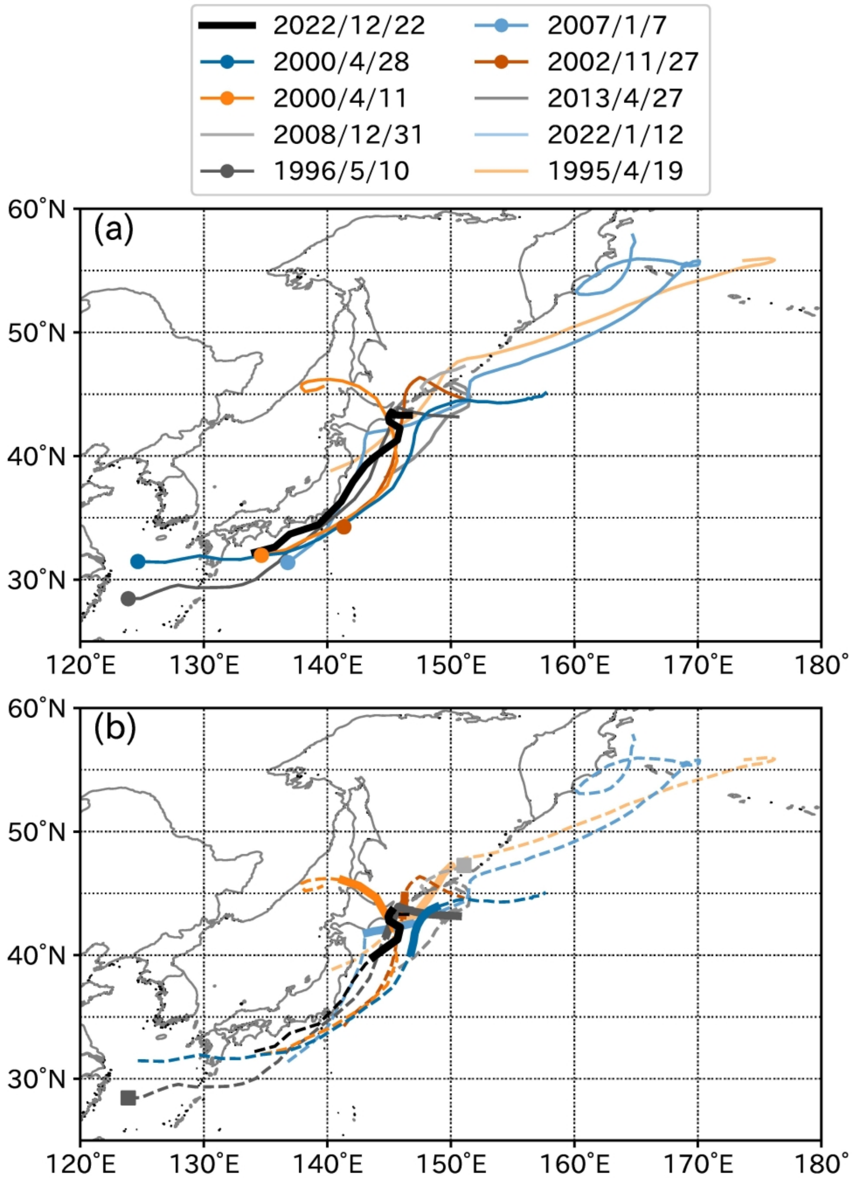

Figure 18. Surface cyclone tracks for the 10 highest SAP events at Monbetsu. In (a), tracks the closest to eastern Hokkaido are illustrated with the December 2022 case highlighted by the thick black line. (b) is identical to (a), except for tracks illustrated with broken lines with periods of suitable temperature for wet snow accretion (0–2 °C) as thick lines. The genesis points are indicated by a circle for tracks of five cyclones exhibiting a similar path to that of the present case in (a), and a square is used for two tracks that exhibit the longest duration (2008/12/31 and 1996/5/10) in (b).

157x217mm (600 x 600 DPI)